University of Copenhagen
FACULTY OF SCIENCE

MATTER AROUND BLACK HOLES: TESTING SCALAR-TENSOR THEORIES OF GRAVITY and PARTICLE EJECTION DURING MERGERS OF DARK MATTER HALOS

Isabella Paola Carucci

Master thesis in Physics

Supervisors:

Steen H. Hansen (DARK, Denmark)

Vitor Cardoso (CENTRA, Portugal)

Dark Cosmology Centre

D Y B H O

August 2013

Abstract

This thesis reports on two distinct investigations: black holes surrounded by matter are studied in scalar-tensor theories of gravity and dark matter particle ejections occurring during halo mergers are analysed through various types of simulations.

In general relativity, stationary asymptotically flat electrovacuum and regular black holes are described by the Kerr-Newman family of solutions; this is still valid in **scalar-tensor theories of gravity**. In this thesis it is shown that within this class of theory exist **two mechanisms which can render black holes unstable** when matter is close-by: the coupling between the scalar field introduced by the theory and matter induces an effective mass for the scalar, changing the dynamics of the system. The square of this effective mass can either be positive or negative according to the specific theory and to the nature of the existent matter. When the effective mass squared is negative and the matter density is above a certain limit, the first mechanism is triggered: the initial general relativity configuration is not stable and the system ends up in a *hairy* state, with the scalar field developing a non-trivial profile. This is a black hole version of **spontaneous scalarization** already studied in neutron stars. The second instability is associated with **superradiance** and is present when the effective mass squared is positive and when the black hole spin exceeds a certain threshold; the amplitude of the unstable modes of the scalar field exponentially grows in time at the expense of rotational energy from the black hole. The second mechanism is also responsible for a resonant effect in the superradiant scattering of monochromatic scalar waves, with amplification factors as large as 10^5 or more, prospecting detectable deviations from general relativity. The phenomena are first analysed analytically in a simplified configuration, then, using simple models for the matter profile around the black hole, a numerical check is done to confirm the emergence of an instability.

Dark matter halos are built from accretion and merging and are believed to be the framework of the present **large scale structure of the universe**. During merging, some of the kinetic energy has to be disposed in order to

reach a new equilibrated configuration. Baryonic matter usually radiates away the energy in excess, dark matter structures relax by expelling some of their particles and let them carry energy away. A consequence of **halo mergers** is indeed the **ejection of particles** with velocities higher than the escape velocity, thus allowing the expelled particles to leave forever the resulting structure. **N-body simulations** and **single-particle smooth-field simulations** are performed in this thesis to demonstrate that this phenomenon is a mean-field effect. Studying a range of minor mergers, it is confirmed that between $5 - 15\%$ of the particles from the smaller of the two merging structures are expelled. It is argued that the rapid changes to the field potential are responsible for such ejection. These findings provide an explanation for the high-velocity component dark matter particles which are observed in cosmological numerical simulations.

Lisbon,
August 1, 2013

Contents

Chapter 1

Introduction

This thesis is composed of two distinct parts: we consider black holes in scalar-tensor theories of gravity and dark matter halo mergers. While these two studies notably differ one from the other (in subject and in modus operandi), they are part of a bigger picture, trying to get a glimpse of the very fundamentals of the universe, as Sir Arthur Eddington put it: *something unknown is doing we don't know what.*

Indeed, while we now have a general picture of the basic constituents that make up the universe (the Planck mission released new data just few months ago: see figure 1.1), there is no understanding of the precise nature of the major components: dark energy, 68.3% and dark matter, 26.8%. Dark energy is related to the accelerated expansion of the universe, dark matter has been hypothesised to fill the discrepancies between the mass of large astronomical objects determined from their gravitational effects and the mass calculated from the luminous (ordinary) matter they contain.

Since the studies on supernovae IA of about 15 years ago, we know that the universe is not only expanding (that was an idea that Hubble and more entertained already in the 1920s) but its expansion is accelerating. Whatever is the *thing* or the mechanism that pushes the universe to ever faster expansion, we call it dark energy. It is sometimes thought as a cosmological constant: a constant energy density filling space homogeneously (Carroll, 2001). It may also be addressed by gravitational physics, such as an extension of general relativity. In the latter we find for instance the **scalar-tensor theories** that, by making the gravitational coupling varying instead of being constant, give a rather general parametrization of dark energy. Moreover, the dynamics of the hypothetical scalar field could account for a unified description of both dark energy and dark matter (Bertacca et al., 2010) and scalar-tensor theories are widely studied also because they can be seen as a low-energy effective version of a more fundamental theory, as string theory, and shed light on quantum gravity. Thus, the interest in scalar-tensor theories is high and supported by different physical sectors.
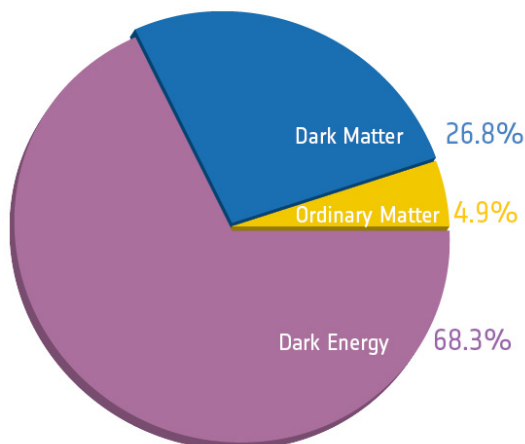
Figure 1.1: The relative amounts of the different constituents of the universe. Image credit: ESA/Planck.

Since in these theories there is one (or more) scalar field mediating the gravitational interaction, one is naturally led to wonder why the scalar field has gone undetected in local and solar system experiments conducted so far. It could be either that the field is massive enough to have just short scale effects (in which case one could not explain the cosmological issues we are interested in) or that it experiences screening mechanisms. This controversy raises the need of considering scalar-tensor theories in strong gravity regime, i.e. within compact stars and black holes, and this is what we focus on in the first part of thesis.

We work with **black holes**: they are simple objects (they are solutions of the Einstein's equations in vacuum) and in general relativity are uniquely described by the Kerr-Newman family of solutions. It has been shown in (Sotiriou and Faraoni, 2012) that these solutions hold also in scalar-tensor theories (just assuming stationarity and asymptotic flatness): the field settles to a constant and the metric still satisfies the Einstein's equations.

If the black holes look the same in general relativity and in scalar tensor theories, how are we going to distinguish them? How can we probe if the scalar field is there or not? We make two considerations:

- dynamically the black holes solutions in the two theories are different: if we perturb the system, the differences should come up

- generically, whenever matter is present, the scalar field is required to assume a nontrivial profile.

Taking these into account, we consider black holes in a scalar-tensor theory placing a matter distribution around them. This configuration has

8

astrophysical relevance, since astrophysical black holes can be surrounded by accretion disks, accretion tori and dark matter halos (Sadeghian et al., 2013).

In chapter 2 we formally set up the system, develop its mathematics and show that an effective mass squared term shows up with coupling the scalar to matter, and it makes possible two different kind of instabilities: one due to **superradiance** and the other called **spontaneous scalarization**. We analyse them in chapters 3 and 4 respectively.

In the following chapters we report on the second study of this thesis, dealing with mergers of **dark matter** halos.

As already introduced above, dark matter is *something* that has to interact with ordinary matter just gravitationally (and that's why it has not been detected so far) and that resides in the whole universe, since evidences come through different observational techniques, spanning different scales. Indeed, the existence of dark matter is motivated

- at the largest scale possible: the size of the **whole universe**. The detection of the power spectrum of the Cosmic Microwave Background (CMB) shows temperature fluctuation $\Delta T/T \sim 10^{-5}$, that is 2 orders of magnitude smaller than the value we expect looking at the present-day structures. If we account for dark matter, that didn't interact electromagnetically with the CMB photons, then structures started forming before CMB seeped out;

- at **large scales**. Spectroscopic redshift surveys measure the spatial distribution of galaxies and how this distribution evolves in time. The outcomes are well fit with the hypothesis of cold dark matter (where *cold* refers to particles travelling with non-relativistic velocities) and with the idea that structure formation proceeds hierarchically, by merging of smaller objects into larger objects (galaxies $\rightarrow$ groups $\rightarrow$ clusters);

- at the **clusters of galaxies** scale: we need dark matter to sum up the mass distribution we measure through the motions of individual galaxies, the distortion of the images of the background galaxies due to dense cluster cores (gravitational lensing) and the measurements of the hot gas temperature, assuming hydrostatic equilibrium;

- at the **galaxies** scale: the rotational curves of the stars don't fall off as if a dark matter halo weren't surrounding the system.

Concluding: dark matter is everywhere and plays a fundamental role in cosmological processes, so the investigation of halos mergers is highly motivated, since it's the brick of structure formation.

In chapter 5 we give an introduction to our work on mergers, explaining why these phenomena cause **particles ejections**, that is what we focus on.

Later we describe how we chose to proceeded: by means of N-body simulations (chapter 6) and by running single-particle smooth-field simulations (chapter 7).

In the last chapter (the 8th) we draw conclusions of both studies reported in the thesis: we sketch the possible observational signatures of the scalar-tensor theories instabilities investigated, and we present the results (and their physical consequences) of the simulations of dark matter halo mergers.

Chapter 2

Framework: the appearance of an effective mass

In this chapter we present the gravitational scalar-tensor theory we consider in the whole work, and we derive all the mathematical equipment we will later need. We show how couplings of scalar field to matter are equivalent to en effective mass for the scalar field, that can be responsible for instabilities.

We use natural units $\hbar = c = G = 1$ and the signature $(-, +, +, +)$ for the metric.

2.1   The action

We work in the context of a general scalar-tensor theory of gravity. Great part of these theories can be described by the following action S (Fujii and Maeda, 2003; Faraoni, 2004)

$$S = \frac{1}{16\pi G} \int d^4x \sqrt{-g} \left(F(\phi)R - Z(\phi)g^{\mu\nu}\partial_\mu\phi\partial_\nu\phi - U(\phi) \right) + S(\Psi_m; g_{\mu\nu}),$$

$$(2.1)$$

where G is a constant, R the Ricci scalar, g the determinant of the metric $g_{\mu\nu}$, $S(\Psi_m; g_{\mu\nu})$ is the action describing all matter fields Ψ_m, minimally coupled to $g_{\mu\nu}$, and ϕ is the scalar field that the theory introduces.

By properly casting the functions $F(\phi)$, $Z(\phi)$ and $U(\phi)$, we recover the specific scalar-tensor theory we want to look at. For example, setting $F(\phi) = \phi$, $G(\phi) = \omega_0/\phi$ and $U(\phi) = 0$ we designate the Brans-Dicke theory (Brans and Dicke, 1961), one of the scalar-tensor theories most widely studied.

The action S in equation (2.1) is written in the Jordan frame, i.e. the scalar field is not minimally coupled to gravity. In order to reduce the gravitational sector of the theory to the canonical Einstein form, we write S

in the Einstein frame, by performing the following conformal transformation

$$g_{\mu\nu}^E = F(\phi)g_{\mu\nu}\,, \tag{2.2}$$

$$\Phi(\phi) = \frac{1}{\sqrt{4\pi}}\int d\phi \left[\frac{3}{4}\frac{F'(\phi)^2}{F(\phi)^2} + \frac{1}{2}\frac{Z(\phi)}{F(\phi)}\right]^{1/2}\,, \tag{2.3}$$

$$A(\Phi) = F^{-1/2}(\phi)\,, \tag{2.4}$$

$$V(\Phi) = \frac{U(\phi)}{F^2(\phi)}\,. \tag{2.5}$$

Here, $A(\Phi)$ is the coupling function, which expresses the strength with which the scalar field Φ interacts with matter, and $V(\Phi)$ the rescaled potential. After these substitutions, the action S in the Einstein frame reads

$$S = \int d^4x\sqrt{-g^E}\left(\frac{R^E}{16\pi} - \frac{1}{2}g_{\mu\nu}^E\partial^\mu\Phi\partial^\nu\Phi - \frac{V(\Phi)}{16\pi}\right) + S(\Psi_m; A(\Phi)^2 g_{\mu\nu}^E)\,. \tag{2.6}$$

We can now derive the equations governing the system, obtaining the analogous version of the Einstein's equation, where the scalar field Φ appears as a source of gravity,

$$G_{\mu\nu}^E = 8\pi\left(T_{\mu\nu}^E + \partial_\mu\Phi\partial_\nu\Phi - \frac{g_{\mu\nu}^E}{2}(\partial\Phi)^2\right) - \frac{g_{\mu\nu}^E}{2}V(\Phi)\,, \tag{2.7}$$

and the Klein-Gordon equation controlling Φ

$$\Box^E\Phi = -\frac{A'(\Phi)}{A(\Phi)}T^E + \frac{V'(\Phi)}{16\pi}\,, \tag{2.8}$$

where we derive the stress-energy tensor $T_{\mu\nu}^E$ in the Einstein frame from the Jordan one using the relation $T_{\mu\nu}^E = A^2(\Phi)T_{\mu\nu}$.

The coupling between the scalar field Φ and the matter acts as a **mass term** in equation (2.8) through the expression $-\frac{A'(\Phi)}{A(\Phi)}T^E$. This is responsible for the mechanisms we investigate in the next chapters, but before moving on that let us simplify the mathematics of the problem.

2.2   A perturbative approach

To better handle equations (2.7) and (2.8), we proceed with a perturbative analysis. We assume the potential $V(\Phi)$ and the coupling function $A(\Phi)$ to be analytical around the background solution Φ_0

$$V(\Phi) = \sum_{n=0} V_n(\Phi - \Phi_0)^n\,, \tag{2.9}$$

$$A(\Phi) = \sum_{n=0} A_n(\Phi - \Phi_0)^n\,. \tag{2.10}$$

We can now expand equations (2.7) and (2.8) in the first order in a small $\varphi \equiv \Phi - \Phi_0 \ll 1$, obtaining

$$G_{\mu\nu}^E = 8\pi \left(T_{\mu\nu}^E + \partial_\mu \Phi_0 \partial_\nu \Phi_0 - \frac{g_{\mu\nu}^E}{2}(\partial \Phi_0)^2 \right) - \frac{g_{\mu\nu}^E}{2}V_0 - \frac{g_{\mu\nu}^E}{2}V_1\varphi$$
$$+ 8\pi \left(\partial_\mu \Phi_0 \partial_\nu \varphi + \partial_\mu \varphi \partial_\nu \Phi_0 - g_{\mu\nu}^E \partial_\mu \Phi_0 \partial^\mu \varphi \right) , \qquad (2.11)$$

$$\Box^E \Phi_0 + \Box^E \varphi = -\frac{A_1}{A_0}T^E + \frac{V_1}{16\pi} + \frac{V_2\varphi}{8\pi} + \varphi T^E \left(\frac{A_1^2}{A_0^2} - 2\frac{A_2}{A_0} \right) . \quad (2.12)$$

With the following considerations, we can cut down equations (2.11) and (2.12) to more concise formulations.

- The term where V_0 appears in equation (2.11) is equivalent to a cosmological constant. We then choose to look at **asymptotically flat solutions** and set $V_0 = 0 = V_1$.

- In equation (2.12), if $A_1 \neq 0$, a constant Φ_0 could not be a possible background solution and we would already face a hairy configuration deviating from what general relativity prescribes. Regardless of whether the theory allows hairless solutions, there exist possible mechanisms that would make a non-trivial Φ profile develop. To point them out, we impose $A_1 = 0$ and we consider a **general relativistic solution as background** Φ_0.

The choice of setting $A_1 = 0$ can appear restrictive. However, since the term $A'(\Phi)/A(\Phi)$ in equation (2.8) has been already constrained by weak gravity experiments and tests for the strong equivalence principle violation to be negligibly small (Damour and Esposito-Farese, 1996, 1998; Freire et al., 2012), we can infer $A'(\Phi_0) \approx 0$, then Φ_0 is an extremum for the function $A(\Phi)$ and $A_1 = 0$ is a motivated assumption.

All that remains of equation (2.12) at the first order in φ is

$$\left[\Box^E - \frac{V_2}{8\pi} + \frac{2A_2}{A_0}T^E \right] \varphi \equiv \left[\Box^E - \mu_s^2(r) \right] \varphi = 0 . \qquad (2.13)$$

We are left with a simple expression for the effective mass μ_s^2 that the scalar field develops in the presence of matter:

$$\mu_s^2(r) \equiv -\frac{2A_2}{A_0}T^E , \qquad (2.14)$$

where we omit the term $\frac{V_2}{8\pi}$ since it is related to a standard mass term of the field Φ and would not change qualitatively our discussion.

The value of the effective mass squared μ_s^2 depends both on the specific scalar-tensor theory, through the constants A_0 and A_2, and on the matter content we deal with, through the trace of the stress-energy tensor T^E. According to the sign of μ_s^2, we later show two distinct effects the system can experience:

13

- $\mu_s^2 = -\frac{2A_2}{A_0} T^E > 0 \implies$ superradiance,

- $\mu_s^2 = -\frac{2A_2}{A_0} T^E < 0 \implies$ spontaneous scalarization.

Superradiant instabilities are related to spinning black holes: their rotation will be slowed down by energy tapping into a scalar field fluctuation. Its end state is still, in principle, a solution of general relativity. Superradiance requires the black hole to be rotating above a certain threshold; interestingly, astrophysical black holes are commonly highly-spinning, so astrophysical observations can be used to put constraints on this instability and, in turn, on scalar-tensor theories.

With spontaneous scalarization we mean that the field equations allow for two solutions: the general relativistic one (with constant scalar field) and another one with a nontrivial scalar profile. The term *spontaneous scalarization* was introduced by Damour and Esposito-Farése in the context of neutron stars to signify that, in a certain region of parameter space, the general relativistic solution is not the preferred one because it is unstable (Damour and Esposito-Farese, 1993).

Chapter 3

Superradiance

When the effective mass μ_s^2 is positive, instabilities due to superradiance can occur. Since superradiance can be experienced only by a spinning black hole, at the beginning of this chapter we review the Kerr solution that describes it and introduce how the extraction of energy takes place. We describe the numerical recipe used to determine the unstable modes and to compute the resonant amplification of scattering waves, within a simple mass distribution model.

3.1   The Kerr black hole

Black holes are the outcome of the gravitational collapse of massive stars. Stars are observed to be rotating , so we expect black holes to possess angular momentum.

In general relativity, the **Kerr metric** $g_{\mu\nu}$ describes the space-time geometry around a massive spinning object (Kerr, 1963) and it is a **unique solution** solving the Einstein equations in vacuum for a rotating black hole (Shapiro and Teukolsky, 1983).

A black hole featuring mass M and angular momentum $J = Ma$ can be described in Boyer-Lindquist coordinates $x^\mu = (t, r, \theta, \phi)$, resulting in the line element ds^2 (Boyer and Lindquist, 1967)

$$ds^2 = g_{\mu\nu}dx^\mu dx^\mu = -\left(1 - \frac{2Mr}{\rho^2}\right)dt^2 - \frac{2Mrasin^2\theta}{\rho^2}2dtd\phi + \frac{\rho^2}{\Delta}dr^2$$
$$+\rho^2 d\theta^2 + \left(r^2 + a^2 + \frac{2Mra^2 sin^2\theta}{\rho^2}\right)sin^2\theta d\phi^2 \, ,$$

$$(3.1)$$

where $\Delta = r^2 + a^2 - 2Mr$ and $\rho^2 = r^2 + a^2 cos^2\theta$ and the black hole rotates in ϕ direction.

Solving the quadratic equation $1/g_{rr} = 0$, we find that the black hole has a coordinate singularity at $r = r_+ = M + \sqrt{M^2 - a^2}$, which corresponds to the event horizon, beyond which no signal can escape.

The metric $g_{\mu\nu}$ reduces to the Schwarzschild metric when $a = 0$, i. e. we recover spherical symmetry when the black hole is not rotating. $g_{\mu\nu}$ is invariant under inversions of t and of ϕ occurring at the same time ($t \to -t$, $\phi \to -\phi$), as time inversion of a spinning body induces the body to spin in the opposite direction.

From the expression of r_+ we infer that the spinning parameter a is bounded from above: the relation $a < M$ has to hold in order for the black hole to exist, i.e. for the metric to display an event horizon and not a naked singularity (which is also supported by the cosmic censorship hypothesis).

Since the rotating black hole is stationary and axial symmetric, the Kerr geometry possesses two killing vectors $t^\alpha = \partial x^\alpha / \partial t$ and $\phi^\alpha = \partial x^\alpha / \partial \phi$. Thus a **stationary observer** (i.e. moving in ϕ as the black hole) with constant angular velocity $\Omega = d\phi/dt$, has four-velocity $u^\alpha = \gamma(t^\alpha + \Omega\phi^\alpha)$, where the γ factor is determined by the normalization $u^\alpha u_\alpha = -1$. In particular, we can calculate the angular velocity Ω_H with which a stationary observer sitting at the event horizon r_+ spins:

$$\Omega_H = \frac{a}{2Mr_+} \,. \tag{3.2}$$

We move on to the case of a **static observer**: its four-velocity is proportional just to the t^α killing vector: $u^\alpha = \gamma t^\alpha$, where γ is again a normalization factor leading to $\gamma^{-2} = -g_{tt} = \left(1 - 2Mr/\rho^2\right)$. Looking at γ we notice that the static observer four-velocity is not timelike in the whole space-time. The static limit is located at $g_{tt} = 0$ and corresponds to the surface

$$r_e = M + \sqrt{M^2 - a^2 cos^2\theta} \,. \tag{3.3}$$

Inside the region $r_+ < r < r_e$, an observer cannot remain static, i.e. it must rotate *with* the black hole. This phenomenon is called frame dragging and the region of space-time where it takes place is known as **ergosphere**. Due to the dependence on θ in r_e, this surface is not spherically symmetric: it looks like a pressed ball along the axis of rotation: at the poles there are the minima for r_e and the surface overlaps the event horizon $r_e(\theta = 0) = r_e(\theta = \pi) = r_+$; at the equatorial plane $\theta = \pi/2$, r_e reaches its biggest value.

3.1.1 Extraction of energy and instability

The existence of the ergosphere is tightly related to the black hole to be spinning: its static counterpart (the Schwarzschild metric) doesn't feature a inertial frame dragging. The ergosphere is seemingly a place where interesting things can happen. Indeed, Penrose was the first to demonstrate that rotational energy can be extracted from a black hole by orbiting and
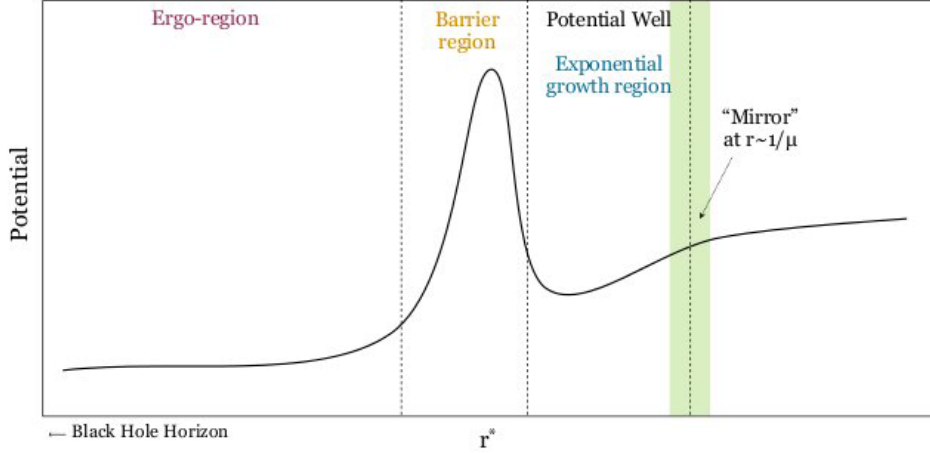
Figure 3.1: The black hole bomb. The shape of the radial part of the potential for the frequency eigenvalue problem. Superradiant modes are localized in a potential well region created by the mass *mirror* from the spatial infinity on the right, and by the centrifugal barrier from the ergoregion and horizon on the left. (Arvanitaki and Dubovsky, 2011).

fissioning particles, through a process that carries his name (Penrose, 1969). Later on, Misner pointed out that waves can also extract rotational energy, thanks to **superradiant scattering**, in which an impinging wave is amplified as it scatters off a rotating black hole (Misner, 1972). He showed that the unstable modes have frequencies ω that satisfy the condition

$$\omega < m\Omega_H \,,$$

with m the azimuthal number.

As an application of superradiance, Press and Teukolsky later considered the system black hole - scalar wave and placed it inside a spherical mirror. In this set-up the superradiantly amplified modes get reflected by the mirror and back towards the black hole, in a tennis-like configuration, ripping some energy from the hole for each bounce and increasing the amplitude exponentially, thus leading to an unstable configuration. They called it the **black hole bomb** (Press and Teukolsky, 1972).

We show how superradiance applies to the system described in chapter 2. The scalar field of the scalar-tensor theory can be superradiantly amplified and the effective mass squared μ_s^2 coming from the coupling to matter, when positive, is a potential barrier that plays the role of a mirror and triggers a black hole bomb-like instability, as shown in figure 3.1.

17

3.2 The wave equation

Let's recall from chapter 2: we consider a black hole in a generic scalar-tensor theory with a matter profile around it; the background field Φ_0 is set to be constant, thus the black hole is described by the Kerr metric $g_{\mu\nu}$ of equation (3.1) and the system is indistinguishable from its general relativistic counterpart.

We want to check the stability of this configuration by acting perturbatively on the field, i.e. we consider a small deviation $\varphi \equiv \Phi - \Phi_0 \ll 1$. In chapter 2 we derived the Klein-Gordon equation (2.13) governing φ, that we now consider with positive μ_s^2, whose value depends on the specific theory and on the matter content, through constants A_0 and A_2 and the stress energy tensor trace T^E:

$$\left[\Box^E - \mu_s^2(r)\right]\varphi = 0\,, \qquad \mu_s^2 = -\frac{2A_2}{A_0}T^E > 0\,. \tag{3.4}$$

We look for separable solutions of the above equation, thus we can express φ as

$$\varphi_\omega = \Psi(r)S(\theta)e^{-i\omega t + im\phi}\,, \tag{3.5}$$

for a specific frequency ω, where $\Psi(r)$ is the radial part, $S(\theta)$ the angular wave function and m the azimuthal number, over which it is implicit the summation. We find that the most generic ansatz for μ_s^2 that separates equation (3.4) is the following

$$\mu_s^2(r,\theta) = \mu_0^2 + 2\frac{\mathcal{F}(\theta) + \mathcal{G}(r)}{a^2 + 2r^2 + a^2\cos 2\theta}\,, \tag{3.6}$$

where μ_0^2 stands as a canonical mass term for a massive scalar, $\mathcal{G}$ and $\mathcal{F}$ are a radial and an angular function respectively. Our point is to qualitatively show the emergence of superradiance, thus the profile above retains enough generality for our purposes.

With the two ansatz in equations (3.5) and (3.6), the Klein-Gordon equation (3.4) splits into a coupled system of equations for the two functions $\Psi(r)$ and $S(\theta)$

$$\frac{1}{\sin\theta}\frac{d}{d\theta}\left(\sin\theta\frac{d}{d\theta}S(\theta)\right)$$
$$+ \left[a^2\left(\omega^2 - \mu_0^2\right)\cos^2\theta - \frac{m^2}{\sin^2\theta} - \mathcal{F} + \lambda\right]S(\theta) = 0\,, \tag{3.7}$$

$$\Delta\frac{d}{dr}\left(\Delta\frac{d\Psi(r)}{dr}\right) + \left[\omega^2(r^2 + a^2)^2 - 4aMrm\omega + a^2m^2\right.$$
$$\left. - \Delta\left(\mathcal{G} + r^2\mu_0^2 + \lambda + a^2\omega^2\right)\right]\Psi(r) = 0\,. \tag{3.8}$$

λ is the separation constant that allows the split of the wave equation and it is found as eigenvalue of equation (3.7); after determining λ, the problem becomes an eigenvalue search for the possible frequencies ω the solution can have.

Looking for complex frequencies $\omega = \omega_R + i\omega_I$, we can identify the instability by focusing on the modes with a positive imaginary part $\omega_I > 0$, which correspond to modes amplitudes exponentially growing in time, as we notice from equation (3.5).

In the limit case of $a \to 0$, the black hole is not rotating, the problem acquires spherical symmetry and we could substitute the terms $S(\theta)e^{im\phi}$ in equation (3.5) with spherical harmonics $Y_{lm}(\theta, \phi)$, with l constant integer $l \geq |m|$. In this case, equation (3.7) is exactly solvable with $\lambda = l(l+1)$. Going back to the $a \neq 0$ case, we can expand λ in powers of $a\omega$

$$\lambda = l(l+1) + \mathcal{O}(a^2\omega^2) \,,$$

the explicit form is in (Seidel, 1989; Berti et al., 2006); in our integration we stop the expansion at the fourth term in $a\omega$ and use it to numerically integrate the radial equation (3.8), as we describe in next section.

3.3 Numerical integration

To better handle equation (3.8), we redefine the radial function $\Psi(r)$ and we introduce the tortoise coordinate r_*

$$\Psi(r) = \frac{R(r)}{\sqrt{r^2 + a^2}}\,, \qquad \frac{dr}{dr_*} = \frac{\Delta}{r^2 + a^2} \,. \tag{3.9}$$

The event horizon r_+ represents a singularity in our coordinate system, but as $r \to r_+$, the tortoise coordinate pushes the horizon to infinity $r_* \to \infty$, so it makes us deal with better behaving functions.

Using the definitions above and setting to zero the canonical mass μ_0^2 that wouldn't change qualitatively the results, equation (3.8) reduces to

$$\frac{d^2}{dr_*^2} R(r) + U R(r) = 0 \,, \tag{3.10}$$

with

$$U = \frac{[\omega(r^2 + a^2) - ma]^2 - \Delta(\lambda + \mathcal{G})}{(r^2 + a^2)^2} - \frac{d}{dr_*} \frac{r\Delta}{(r^2 + a^2)^2}$$
$$- \frac{r^2\Delta^2}{(r^2 + a^2)^4} \,. \tag{3.11}$$

Near the boundaries of interest, i.e. the black hole horizon and spatial infinity, the scalar field behaves as

infinity: $r_* \to +\infty$, $\Psi \sim e^{+i\omega r_*}$, outgoing (compact domain),

horizon: $r_* \to -\infty$, $\Psi \sim e^{-i(\omega - m\Omega_H)r_*}$, ingoing (the only physically acceptable solution).

By looking at the incoming wave at the horizon, it is evident that in a superradiant regime, since $\omega < m\Omega_H$, the field would appear outgoing to an inertial observer at spatial infinity, and energy is indeed being extracted.

Considering the boundary conditions above, we can write the solution $R(r)$ at the boundaries as series expansions (Dolan, 2007). At the event horizon, we have

$$R_h(r) = e^{-i(\omega - m\Omega_H)r_*} \sum_0^N h_i(r - r_+)^i \,, \tag{3.12}$$

and at spatial infinity

$$R_{\text{inf}}(r) = e^{i\omega r_*} \sum_0^N \frac{g_i}{r^i} \,. \tag{3.13}$$

The expressions of coefficients h_i and g_i are determined straightaway assuming that the matter profile doesn't have support in the asymptotic regions. The typical order of the series is 3 and 7, for the horizon and infinity respectively. These values are increased when there is the need to double-check an ambiguous result, since they directly affect the accuracy of the integration, although slowing down the computation.

Using the expansion R_{inf}, we can write a generic solution as

$$R_{\text{gen}}(r) = e^{i\omega r_*} \left(A_{\text{out}} + \sum_1^N \frac{g_i}{r^i} \right) + e^{-i\omega r_*} \left(A_{\text{in}} + \sum_1^N \frac{g_i}{r^i} \right) \,, \tag{3.14}$$

where we combined the two possibilities: an outgoing field with coefficient A_{out} and an ingoing characterised by A_{in}.

We numerically integrate in r the homogeneous radial equation equation (3.10) starting from the horizon at $(1 + \epsilon)r_+$, where we adopt an indicative value $\epsilon = 10^{-4}$, using the series in equation (3.12). We integrate outward until a large value of $r = r_{\text{inf}}$, the assigned spatial infinity. We check the accuracy of the integration by varying the value of r_{inf}, that can range from $3/\omega$ to $100/\omega$, until getting typically a 10^{-5} accuracy, i.e. when different r_{inf} values yield to the same result up to the fifth decimal digit.

We finally find the coefficients A_{in} and A_{out} of equation (3.14) by matching the numerical solution at r_{inf} with our generic solution R_{gen}. We build a function that for every different frequency ω returns the value of A_{in}. In order to satisfy our boundary condition at infinity, i.e. having just an outgoing field, we look for zeros of the function: the frequencies such that $A_{\text{in}} = 0$.

Another consequence of looking for unstable modes is that the radial solution Ψ is spatially confined for $\omega_I > 0$, so we can plot the absolute value $|\Psi|$ of the numerical solution after each integration to check if it goes to zero at $r \to r_{\text{inf}}$. Most of the time a better guess of the numerical infinity r_{inf} improves the outcome of this check.

In the next section we show the results of the numerical integration with some specific profile for $\mu_s^2(r, \theta)$. Before starting to integrate with the specific profile, the code has been checked with $\mu_s^2 = 0$ and $\mu_s^2 = constant$, and confronting the frequencies obtained for different modes with the values already known in literature, e.g. in (Leaver, 1985; Cardoso and Yoshida, 2005; Dolan, 2007).

3.3.1 Spherically symmetric model

We look for unstable modes of the scalar field perturbation φ using a spherically symmetric matter profile, thus with $\mu_0^2 = 0$ and $\mathcal{F}(\theta) = 0$

$$\mu_s^2 = 2\frac{\beta\Theta(r - r_0)r^{-n}(r - r_0)}{a^2 + 2r^2 + a^2\cos 2\theta} \,, \tag{3.15}$$

with $\Theta(r)$ the step function. This profile retains two important characteristics we expect matter structures around black holes have: it displays an inner surface characterised by the radius r_0 and falls down at large radii with steepness dictated by the parameter n.

The constant β includes information both on the scalar-tensor theory and on the matter density of the *accretion halo*, since we are not aware of the specifics of these. Thus we carry a general and qualitative discussion.

In figures 3.2 to 3.5 we summarise the results showing just the unstable modes found. All the plots refer to $l = m = 1$ modes, for which the effect is stronger and easier to numerically track. The spinning parameter is set to be $a = 0.99$, since astrophysical black holes are observed to be highly spinning (McClintock et al., 2006). We use two different falloffs: $n = 3$ and $n = 4$. For each of them we track some unstable modes for fixed β and increasing r_0 and the other way around.

In all figures the top panel refers to the real part of the frequency ω_R and the bottom to the imaginary ω_I. In the ω_R plots we highlight with a dotted line the superradiant limit $m\Omega_H$; it is very clear that it is indeed when the real part of the frequency gets below the limit that the instability arise since the imaginary part becomes positive $\omega_I > 0$.

Looking at the plots with varying r_0 it is noticeable that a minimum r_0 is needed for the instability to take place; this is expected since the possible frequencies scale as $\omega \sim 1/r_0$, so for too small r_0 the superradiant condition wouldn't be fulfilled.

In the plots with varying β: the instability rate grows with β up to some value, after which β increases without a remarkably effect on ω_I. This is akin
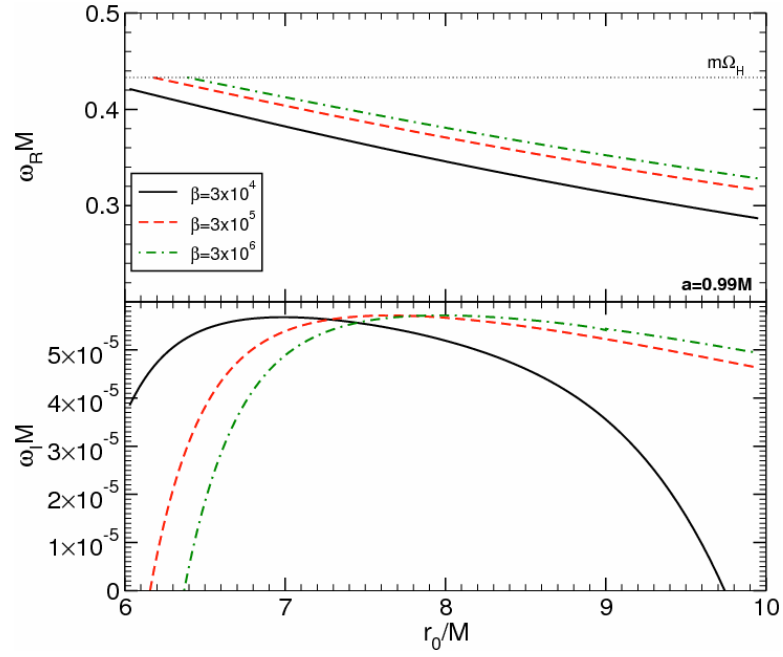
Figure 3.2: Superradiant unstable modes for an $n = 3$ profile and different values of β.

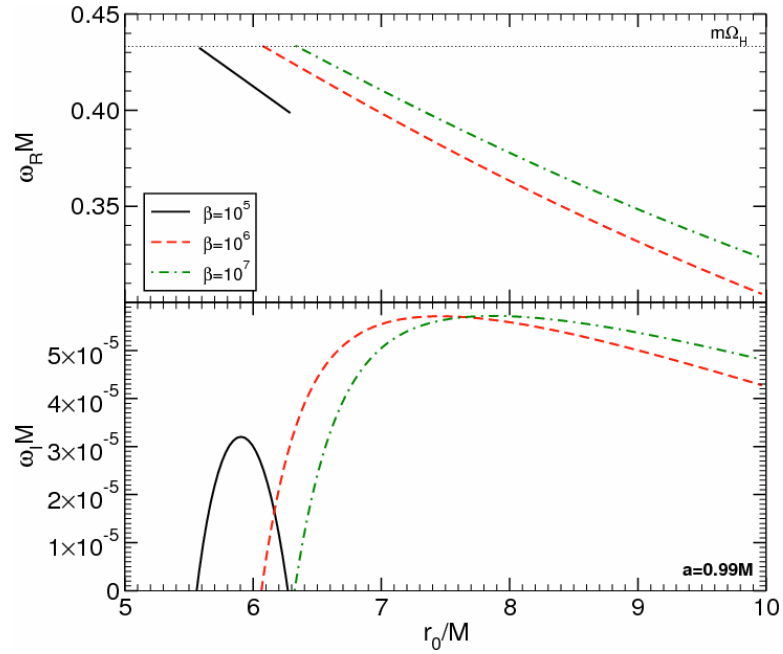

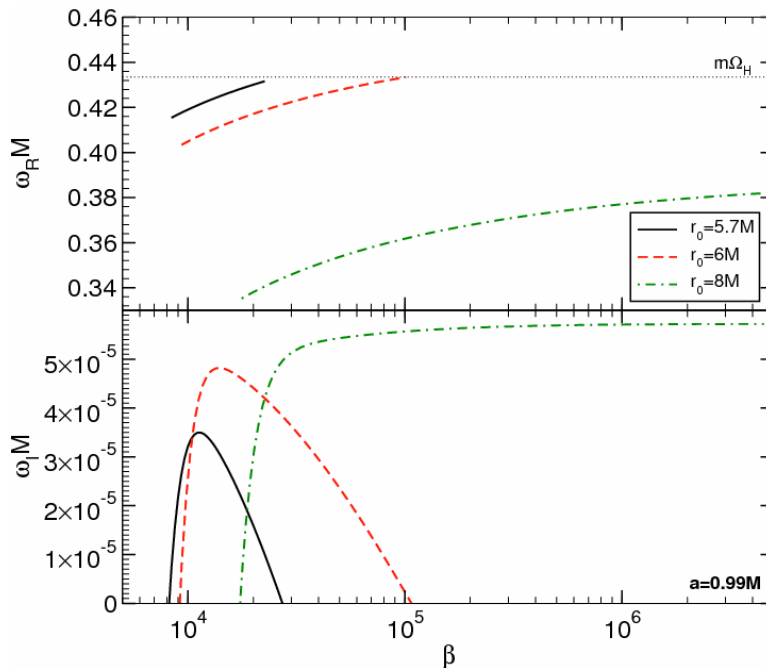Figure 3.3: Superradiant unstable modes for an $n = 4$ profile and different values of β.

Figure 3.4: Superradiant unstable modes for an $n = 3$ profile and different values of r_0.

of the *black hole bomb*: when the potential barrier is high enough to trap the field, an even higher barrier doesn't change qualitatively the mechanism (Cardoso et al., 2004).

The growing scale of the instability is $\tau \sim 1/\omega_I$, so higher values of ω_I signal faster growing instability (i.e. every $1/\omega_I$ the amplitude of the field gets approximately doubled). But as the unstable mode grows, the black hole slows down (Ω_H decreases) and ω_R will eventually overcome the superradiant limit and end up in a stable state.

3.3.2 Resonant amplification

Besides the instability described previously, superradiance is related to another phenomenon that could leave possible observational signatures: the **scattering of monochromatic waves**.

We have already seen that the physical ingoing asymptotic solution at the horizon $\Psi \sim e^{-i(\omega - m\Omega_H)r_*}$ corresponds to a *coordinate outgoing* wave when $\omega < m\Omega_H$, i.e. the wave has to be physically ingoing in the frames of all physical observers, who would be all dragged around the hole by its rotation. For example, let us consider an incident wave on the black hole; generally, part is reflect from the potential barrier (the central peak in the illustration 3.1) and part seeps down over the event horizon, so the resulting outgoing
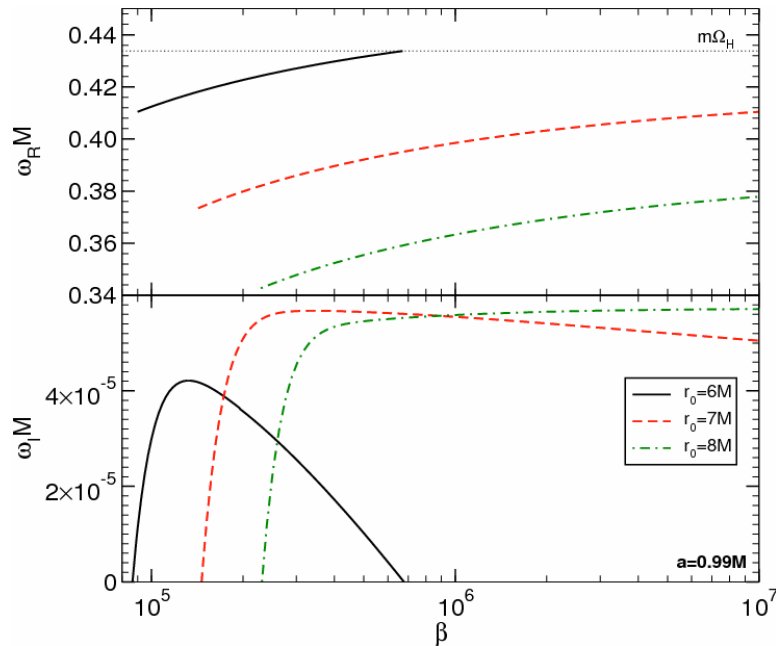
Figure 3.5: Superradiant unstable modes for an $n = 4$ profile and different values of r_0.

wave is weaker than the original. When the superradiant condition holds, the wave who passes through the barrier comes back too and sums up to the barrier reflected wave, so we eventually experience more outgoing energy than ingoing, at the expense of black hole rotational energy (Bekenstein, 1973).

In the context of general relativity the amplification of the scalar field is low: of the order of few tenths percent in energy, at most 0.4% (Press and Teukolsky, 1972). We here show that amplification within scalar-tensor theories can be remarkably substantial.

Our modus operandi is close to what done for the *bomb* case: we numerically solve equations (3.7) and (3.8) with the spherical profile (3.15). We can re-write the usual boundary conditions in the following way

$$\Psi \sim \begin{cases} \mathcal{T}e^{-i(\omega - m\Omega_H)r_*} & r_* \to -\infty \\ e^{-i\omega r_*} + \mathcal{R}e^{i\omega r_*} & r_* \to \infty \end{cases}, \tag{3.16}$$

describing an incident wave of amplitude normalised to unity from spatial infinity giving rise to a reflected wave of amplitude $\mathcal{R}$ and a transmitted wave of amplitude $\mathcal{T}$ at the horizon. Plugging the asymptotic solutions into the master equation (3.10), we can derive

$$(\omega - m\Omega_H)|\mathcal{T}|^2 = \omega(1 - |\mathcal{R}|^2),$$
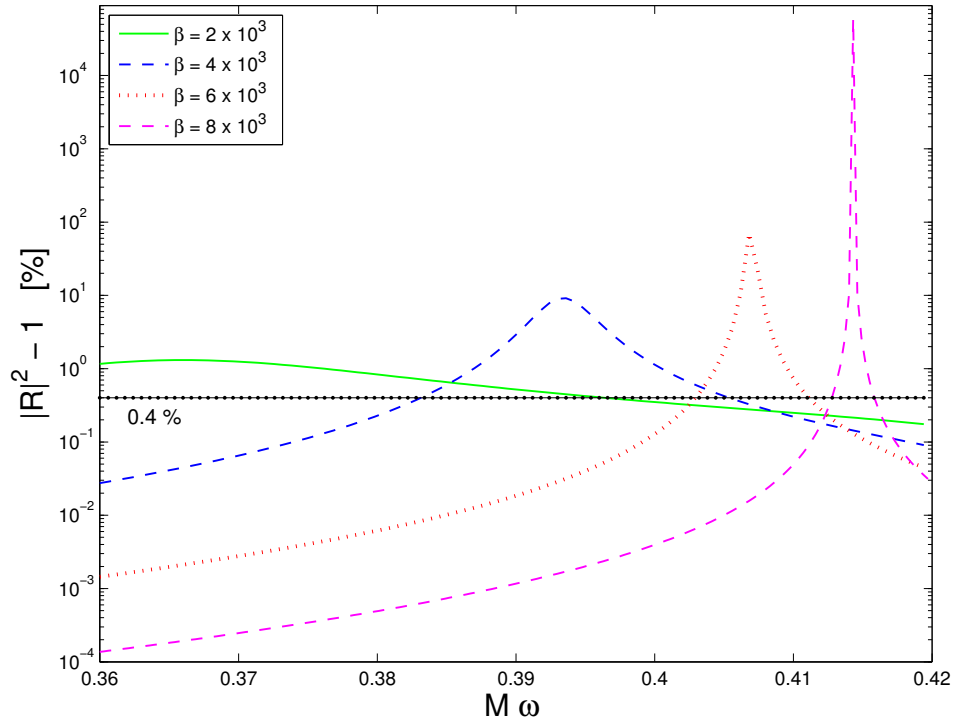
24

Figure 3.6: Amplification factor (in percentage) as function of the frequency for a scalar field scattered off a Kerr black hole with $a = 0.99$ and matter profile featuring $r_0 = 5.7M$ and different values for β, for the $l = m = 1$ mode. The black horizontal dashed line refers to the maximum superradiant amplification in general relativity in vacuum.

where it is once again clear that when we are in a superradiant regime ($\omega < m\Omega_H$), than $|\mathcal{R}|^2 > 1$, i.e. the amplitude of the reflected wave is larger than the incident amplitude.

We define the gain factor as $|\mathcal{R}|^2 - 1$. In figure 3.6 we summarise the results of the integration for a black hole with $a = 0.99$ and matter profile with $r_0 = 5.7M$ with various β values, although similar plots hold for different parameters. We notice that for high enough β, the gain factor can be up to 6 orders of magnitude bigger than the standard value (dashed line in the plot 3.6).

We can use the outcomes of the previous superradiant instability analysis to better interpret these results regarding amplification. For example, looking at figure 3.4 we notice that, within the same parameters for β and r_0, the frequency range in figure 3.6 refers to stable modes, so we are sure we are looking at amplification of monochromatic waves.

From equation (2.14), we expect $\beta \propto A_2/A_0$ and the latter quantity is currently constrained just from below (Damour and Esposito-Farese, 1996). Since the amplification effect is related to big β's, it could be important in framing scalar-tensor theories. These relevant gain factor values correspond to resonant-like peaks for particular frequencies. It's again the previously analysis done for the instabilities that helps us explaining this *spike* effect: we found that modes with $\omega_I = 0$ exist, e.g. in figure 3.4 this happens for $\beta \approx 8194$ and $r_0 = 5.7M$, where we only have a real component $\omega_R \approx 0.4149/M$. $\omega = \omega_R$ modes never die off (since $\Psi_t \sim e^{-i\omega t}$), so would be forever amplified. The latest case would require an incredible fine-tuning, nevertheless it shows what's behind the spikes in the plot 3.6.

Chapter 4

Spontaneous scalarization

When the effective mass μ_s^2 is negative and below a certain threshold, the black hole hairless configuration is unstable and a non-zero scalar field is spontaneously excited. This is the direct analog of the spontaneous scalarization studied for compact stars in scalar-tensor theory (Damour and Esposito-Farese, 1993, 1996; Pani et al., 2011; Barausse et al., 2012).

In this chapter we first consider the non-rotating case: we compute a lower bound for μ_s^2 necessary to trigger the phenomenon and we analytically derive the possible end-states of the instability. We numerically study the rotating case.

4.1   The spherically symmetric case

For simplicity, let us work in a polar coordinate system (t, r, θ, ϕ) with a spherically symmetric matter profile $T^E = T^E(r)$ that has a negligible back-reaction in the geometry. These assumptions allow us to adopt a Schwarzschild background metric of a black hole of mass M

$$ds^2 = -\left(1 - \frac{2M}{r}\right) dt^2 + \frac{1}{(1 - \frac{2M}{r})} dr^2 + r^2(d\theta^2 + \sin\theta^2 d\phi^2) \qquad (4.1)$$

and to decompose the field φ into spherical harmonics

$$\varphi(t, r, \theta, \phi) = \sum_{lm} \frac{\Psi_{lm}(r)}{r} e^{-i\omega t} Y_{lm}(\theta, \phi) \,. \qquad (4.2)$$

Using the definitions in equations (4.1) and (4.2) we can reduce the Klein-Gordon equation (2.13) in a one dimensional ordinary differential equation of a Schrödinger type for the radial part $\Psi(r)$ of the field (hereafter the

angular subscript lm is implicit).

$$\frac{d^2\Psi(r)}{dr_*^2} + \left[\omega^2 - \mathcal{V}(r)\right]\Psi(r) = 0\,, \tag{4.3}$$

$$\mathcal{V}(r) = f\left(\frac{l(l+1)}{r^2} + \frac{2M}{r^3} + \mu_s^2(r)\right). \tag{4.4}$$

where we define the tortoise coordinate r_* as $dr/dr_* = f = 1 - 2M/r$.

Given the expression for $\mu_s^2(r)$ and proper boundary conditions, we are left with a eigenvalue problem for the possible frequencies ω the solutions have. It is clear from the time dependence of φ in equation (4.2) that an exponentially growing instability shows up whenever the imaginary part of the frequency assumes positive values $\omega_I > 0$.

4.1.1 The threshold of the instability

In the case of spontaneous scalarization in neutron stars, the instability arises when the central pressure of the star goes above a certain threshold. We expect something similar to happen in our configuration, where we deal with the density of the matter surrounding the black hole.

The potential $\mathcal{V}$ in equation (4.3) is unidimensional and dies off at spatial infinity, thus we can use the quantum mechanical results in (Buell and Shadwick, 1995) in order to have a rough quantitatively idea of when spontaneous scalarization is triggered. Indeed, a **sufficient condition** for $\mathcal{V}$ to lead to an instability is

$$\int_{2M}^{\infty} \frac{\mathcal{V}}{f} dr < 0\,. \tag{4.5}$$

Looking at equation (4.4), we notice that it is the $\mu_s^2(r)$ negative contribution that could make the potential $\mathcal{V}$ satisfy the condition above. We are indeed dealing with an instability that arises when $\mu_s^2 = -\frac{2A_2}{A_0}T^E < 0$. Substituting the expression for μ_s^2, equation (4.5) reads

$$2\frac{A_2}{A_0}\int_{2M}^{\infty} T^E dr > \frac{2l(l+1)+1}{4M}\,. \tag{4.6}$$

This is a rather general analytical result that we can employ with some simple theoretical models.

Simple models

Let us start by considering a constant density spherical shell of thickness L surrounding the hole at distance r_0. It is described by

$$\mu_s^2 = -\frac{\beta}{M^2}\left(\Theta(r - r_0) - \Theta(r - r_0 - L)\right), \tag{4.7}$$

with $\Theta(r)$ the step function. This profile doesn't allow matter to be closer than r_0 to the black hole, as it indeed happens to astrophysical objects as accretion disks. r_0 could assume for example the value of the ISCO, the black hole innermost stable circular orbit. The constant β sums up the contribution of the scalar-tensor theory constants and the information on the matter density.

Plugging the model of equation (4.7) into equation (4.6), we determine a sufficient condition for the instability to occur within this specific matter profile

$$\beta \gtrsim \frac{2l(l+1)+1}{4}\frac{M}{L} \ . \tag{4.8}$$

Already this simple result shows that a minimum matter density is necessary to experience instabilities, like in the compact stars case. This is dynamically favoured as we can imagine the matter accreting around the black hole at first with small enough mass for the system to be described by general relativity and then eventually reaching the threshold for these solutions to be spontaneously scalarized.

Moving to a more sophisticated model, let us examine the following

$$\mu_s^2 = -\Theta(r-r_0)\beta M^{n-3}\frac{r-r_0}{r^n} \ . \tag{4.9}$$

Besides the existence of an inner surface, in this profile matter is arranged such that it radially fades off, so it eventually decays to zero assigning a proper n parameter. In details, there is no matter at radii $r < r_0$, than the density peaks at $r = n/(n-1)r_0$ and decay $\sim r^{1-n}$ at large distances.

Within this profile, spontaneous scalarization occurs for

$$\beta \gtrsim \frac{2l(l+1)+1}{4}(n-2)(n-1)\left(\frac{r_0}{M}\right)^{n-2} \ . \tag{4.10}$$

We are now able to check the fairness of the condition borrowed from quantum mechanics, illustrated by equation (4.5). We integrate numerically equation (4.3) substituting μ_s^2 with equation (4.9). We adopt the boundary conditions

infinity $r_* \to +\infty$ $\Psi \sim e^{+i\omega r_*}$, outgoing waves (compact domain),

horizon $r_* \to -\infty$ $\Psi \sim e^{-i\omega r_*}$, ingoing waves (the only physically acceptable solution).

and we use a code akin to the one described in section 3.3. We track the unstable modes thus found changing the constant β. A sample of the results is shown in figure 4.1, plotting just the imaginary part ω_I for three different l modes since $\omega_R = 0$. On the x-axis we highlight with dots of the corresponding colours the threshold values determined by equation (4.10) and

notice that are in the instability range: indeed equation (4.5) is a *sufficient* condition for spontaneous scalarization to occur.

The instability connected to spontaneous scalarization is characterised by purely imaginary modes, as $\omega_R = 0$ for all values of β.
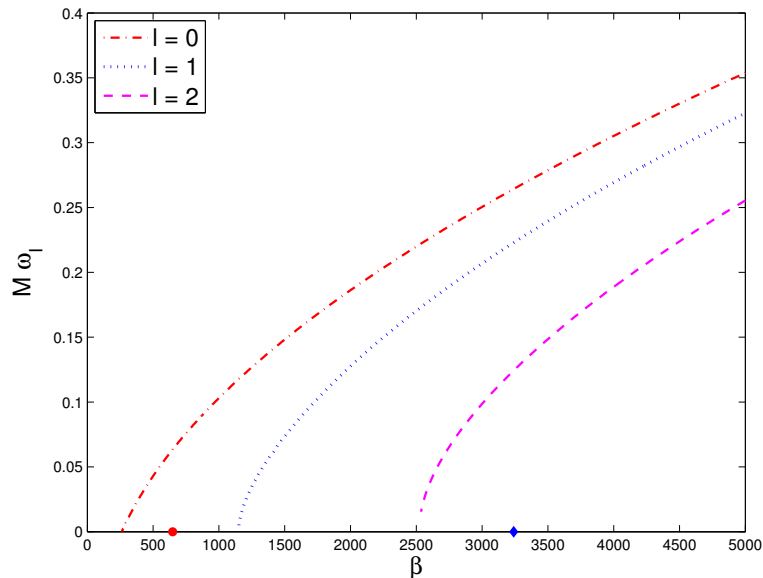

Figure 4.1: Unstable modes for a Schwarzschild background in a scalar-tensor theory surrounded by a matter profile as in equation (4.9) with $n = 5$ and $r_0 = 6\,M$, for different modes l. The red dot and the blue diamond correspond to the threshold values calculated through equation (4.10) for the $l = 0$ and $l = 1$ modes (the respective $l = 2$ value lays outside the $\beta-$range of the graph).

Constraints on the matter distribution

Using a dust approximation with negative $T^E \sim -\rho$, with ρ the matter density, we need a negative $\frac{A_2}{A_0}$ for the instability to arise. Binary pulsar experiments already constrain scalar tensor theories parameters from below (Damour and Esposito-Farese, 1996)

$$\frac{A_2}{A_0} \gtrsim -26\,. \tag{4.11}$$

Since we are assuming $T^E \sim -\rho$ we can rewrite the conditions for β in equations (4.8) and (4.10) in terms of the mass μ of the spherical distribution (for the second model, its finiteness requires $n > 4$)

$$\mu = 4\pi \int T^E r^2 dr,$$

getting respectively for the two models

$$-\frac{A_2}{A_0}\frac{\mu}{M} \gtrsim \frac{2l(l+1)+1}{6}\frac{3r_0(r_0+L)+L^2}{M^2}\,, \tag{4.12}$$

$$-\frac{A_2}{A_0}\frac{\mu}{M} \gtrsim 2\pi\frac{2l(l+1)+1}{2}\frac{(n-2)(n-1)}{(n-4)(n-3)}\left(\frac{r_0}{M}\right)^2\,. \tag{4.13}$$

We can use the maximum value allowed (in absolute value) for A_2/A_0 to have an idea of *how much matter* is necessary to activate spontaneous scalarization. We pick the $l=0$ mode and approximate the first model with $L \ll r_0$ and the second with $n \gg 1$ and we get the requirement

$$\frac{\mu}{M} \gtrsim 0.1\left(\frac{r_0}{M}\right)^2\,. \tag{4.14}$$

4.1.2 Is the assumption of a Schwarzschild background consistent?

In the previous toy models, we assume that the background metric is that of a Schwarzschild black hole, even in the presence of matter; this would require $\mu \ll M$, which barely fits the requirement in equation (4.14). Anyways, spontaneous scalarization is a pretty generic effect and we now show it takes place also in more consistent frameworks.

Let us examine a spherically symmetric black hole surrounded by a spherically thin shell at distance R. There is an exact solution of Einstein's equation and the metric reads

$$ds^2 = -(1-2m(r)/r)dt^2 + (1-2m(r)/r)^{-1}dr^2 + r^2d\Omega^2\,, \tag{4.15}$$

where

$$m(r) = \begin{cases} M & \text{for } r \geq R \\ M_{\text{int}} & \text{for } r < R. \end{cases}$$

We assume the shell to be composed by perfect fluid and to be spatially two-dimensional, then the surface stress-energy tensor reads

$$S_{ab}^E = \sigma u_a u_b + P(\gamma_{ab} + u_a u_b)\,, \tag{4.16}$$

with P the pressure and σ the surface energy density, γ_{ab} the induced metric on the shell and u_a the on-shell four-velocity, all quantities referring to the Einstein frame. It follows that the stress-energy tensor trace reads

$$T^E = S\delta(r-R) = S_{ab}^E\gamma^{ab}\delta(r-R) = (2P-\sigma)\delta(r-R)\,. \tag{4.17}$$

The Israel's junction conditions provide and expression for the internal mass M_{int} and R in terms of σ, P and M (Israel, 1966).

31

In this system, the sufficient condition for spontaneous scalarization in equation (4.5) reads

$$2\frac{A_2}{A_0}(2P - \sigma) > \frac{2l(l+1)+1}{4M_{\text{int}}} + \frac{M - M_{\text{int}}}{R^2} > 0\,, \tag{4.18}$$

which reduces to the second model previously discussed when $M_{\text{int}} = M$.

In this case, the appearance of the instability is related to the thermodynamical properties of the matter distribution. According to the sign of A_2/A_0, we could either require $\sigma > 2P$ or $\sigma < 2P$.

4.2 The case of a rotating black hole

To look for unstable modes due to spontaneous scalarization in a Kerr background, we adopt the numerical integration described in section 3.3, using the spherically symmetric mass distribution in equation (3.15) and considering a negative constant β (in order to have $\mu_s^2 < 0$).

Results are summarised in figures 4.2 and 4.3, with ω_R in the top plot and ω_I in the bottom, for different values of β and different matter position r_0. As we already found in the Schwarzschild case, the denser the matter distribution, the stronger is the instability, which in our case is related to bigger values of $|\beta|$ that correspond to higher frequency imaginary part ω_I. Moreover, high instability is also related to small values of r_0, thus to the vicinity of matter to the black hole.

Unlike the superradiant modes found in chapter 3, in the spontaneous scalarized case we cannot track unstable modes beyond $\omega_I = 0$, i.e. the modes are unstable per se.

4.3 The final state

Once verified that general relativistic solutions can be unstable when $\mu_s^2 < 0$, we want to understand towards what configurations the system approaches to overcome the instability. Our strategy is to look for the possible stationary hairy solutions to the field equations that retain the same symmetry of the initial problem, skipping this way a non-linear time evolution. We choose to operate in two ways: adopting the Israel's formalism to describe the thin shell (Israel, 1966) and by a perturbative analysis, then we numerically integrate and compare the results.

Israel's junction approach

Let us go back to the spherically symmetric case, considering a spherical thin shell of matter. The space-time we deal with is described by

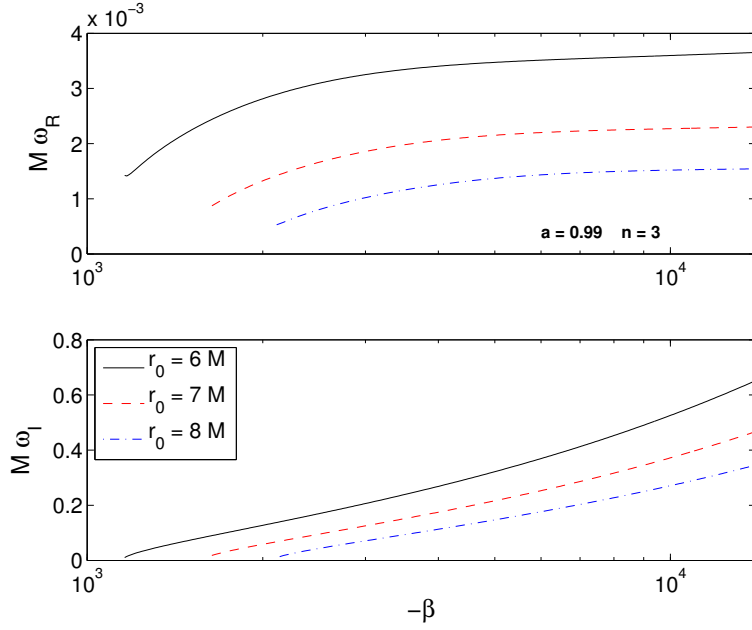$$ds^2 = -h(r)dt^2 + f(r)^{-1}dr^2 + r^2(d\theta^2 + sin^2\theta d\phi^2) \tag{4.19}$$

Figure 4.2: Spontaneous scalarization. Unstable modes for an $n = 3$ profile and different values of r_0, $l = m = 1$, $a = 0.99$.
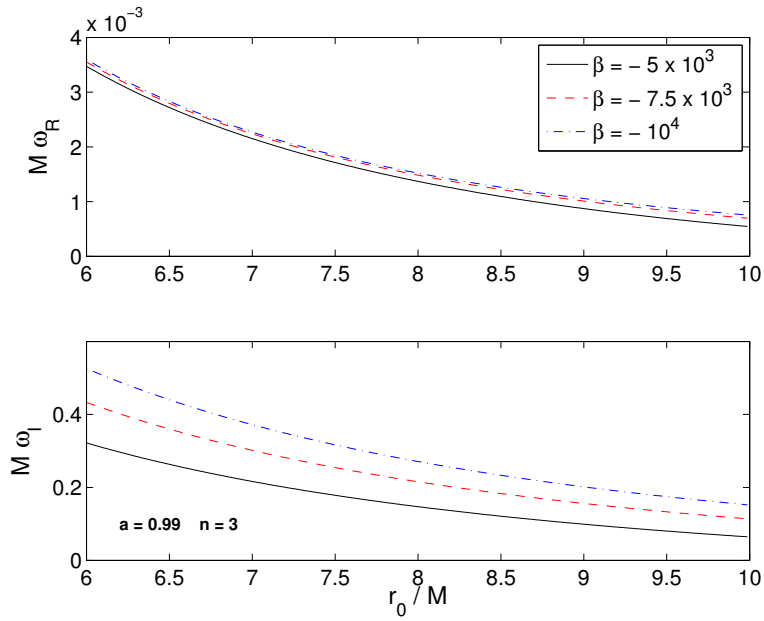

Figure 4.3: Spontaneous scalarization. Unstable modes for an $n = 3$ profile and different values of β, $l = m = 1$, $a = 0.99$.

with h and f functions of the radius r only.

Since we consider a zero-thickness shell of matter distribution, $T^E = 0$ everywhere: the Klein-Gordon equation (2.8) for the original field $\Phi = \Phi_0 + \varphi$ reduces to

$$\frac{d\Phi}{dr} = \frac{Q}{r^2\sqrt{fh}}, \tag{4.20}$$

where Q is the scalar charge that is function of the shell composition (surface density σ and pressure P) and of the scalar-tensor theory (coupling function $A(\Phi)$). Indeed, using the stress-energy tensor trace in equation (4.17), the full equation (2.8) reads

$$\frac{d}{dr}\left(r^2\sqrt{hf}\Phi'\right) = -\frac{A'(\Phi)}{A(\Phi)}S\delta(r - R). \tag{4.21}$$

And integrating it across the shell we determine

$$Q = \left.\frac{A'}{A}\right|_R (\sigma - 2P), \tag{4.22}$$

where A' and A are to be evaluated at the shell's location, $r = R$.

Hence, the charge Q is uniquely determined by the thermodynamical properties of the shell σ and P and the value of the field at the shell position $\Phi(R)$. As expected, when A' vanishes at the radius then $Q = 0$, i.e. when $\Phi(R) = \Phi_0$. In this case, the scalar field is constant through the entire space-time and the solution reduces to its general relativistic counterpart, with constant Φ_0 in the background.

Using the metric in equation (4.19) and Φ' in (4.20), we are able to solve the Einstein's equations in (2.7). The tt and rr components yield

$$4\pi Q^2 + r^2 h \left(f + rf' - 1\right) = 0, \tag{4.23}$$
$$4\pi Q^2 + r^2 h \left(1 - f\right) - r^3 fh' = 0, \tag{4.24}$$

the other two components are linear combinations of the equations above.

To express the jump in the metric as function of the shell thermodynamical properties, we borrow again the results in (Israel, 1966). For a static shell at $r = R$ it holds

$$\sigma = -\frac{1}{4\pi R}\left(\sqrt{f_+} - \sqrt{f_-}\right), \tag{4.25}$$
$$P = \frac{1}{8\pi R}\left(-4\pi R\sigma + \sqrt{f_+}\frac{Rh'_+}{2h_+} - \sqrt{f_-}\frac{Rh'_-}{2h_-}\right). \tag{4.26}$$

Now we are able to integrate equations (4.23) and (4.24) from spatial infinity to the the shell, then we use equations (4.25) and (4.26) as matching conditions and keep integrate up to the Schwarzschild interior.

Perturbative approach

Let us consider the metric describing the space-time in the limit of a small scalar charge Q

$$ds^2 = -\left(1 - \frac{2M}{r} + H\right)dt^2 + \frac{1}{1 - \frac{2M}{r} + F}dr^2 + r^2(d\theta^2 + sin^2\theta d\phi^2) , \quad (4.27)$$

where H and F are functions of r. We know in the interior (inside the shell) the metric is Schwarzschild so $\Phi = constant$ has to hold (as for all general relativistic solutions); it follows that

$$H = F = C/r.$$

To determine H and F in the exterior, we impose asymptotic flatness, i.e. the metric becomes flat at large radii, and we get

$$\Phi' = \frac{Q}{r(r - 2M)} , \quad (4.28)$$

$$F = \frac{2\pi Q^2}{Mr} \log\left(\frac{r}{r - 2M}\right) , \quad (4.29)$$

$$H = -\frac{2\pi Q^2}{M^2 r}\left[2M + (r - M)\log\left(\frac{r - 2M}{r}\right)\right] , \quad (4.30)$$

with M the total mass in the Einstein frame, which is different from the Schwarzschild interior mass, that can be derived from the event horizon r_h

$$M_{\text{int}} \equiv \frac{r_h}{2} = \frac{2M - C}{2} . \quad (4.31)$$

At large distances, it can be derived from equation (4.28) that $\Phi \sim Q/r$; in the physical Jordan frame, this corresponds to a shell with an effective scalar charge $\propto Q$. Indeed, using equation (2.2) and the expansion in (2.10), the large-distance expansion of the metric g_{tt} in the Jordan frame reads

$$-g_{tt} = 1 - \frac{2M - 2A_1 Q}{r} + \frac{A_1^2 Q^2 - 2A_1 MQ + 2A_2 Q^2}{r^2} . \quad (4.32)$$

Therefore, in theories with $A_1 \neq 0$ the scalar field contributes to the total physical mass. Furthermore, the space-time acquires a scalar charge given by the coefficient of the $1/r^2$ term above. When $A_1 = 0$, the scalar charge is proportional to $\sqrt{A_2}Q$.

We now have a well defined problem: the scalar charge Q is determined by the matter composition parameters σ and P and the equations above allow us to derive the metric components and the possible field profiles.
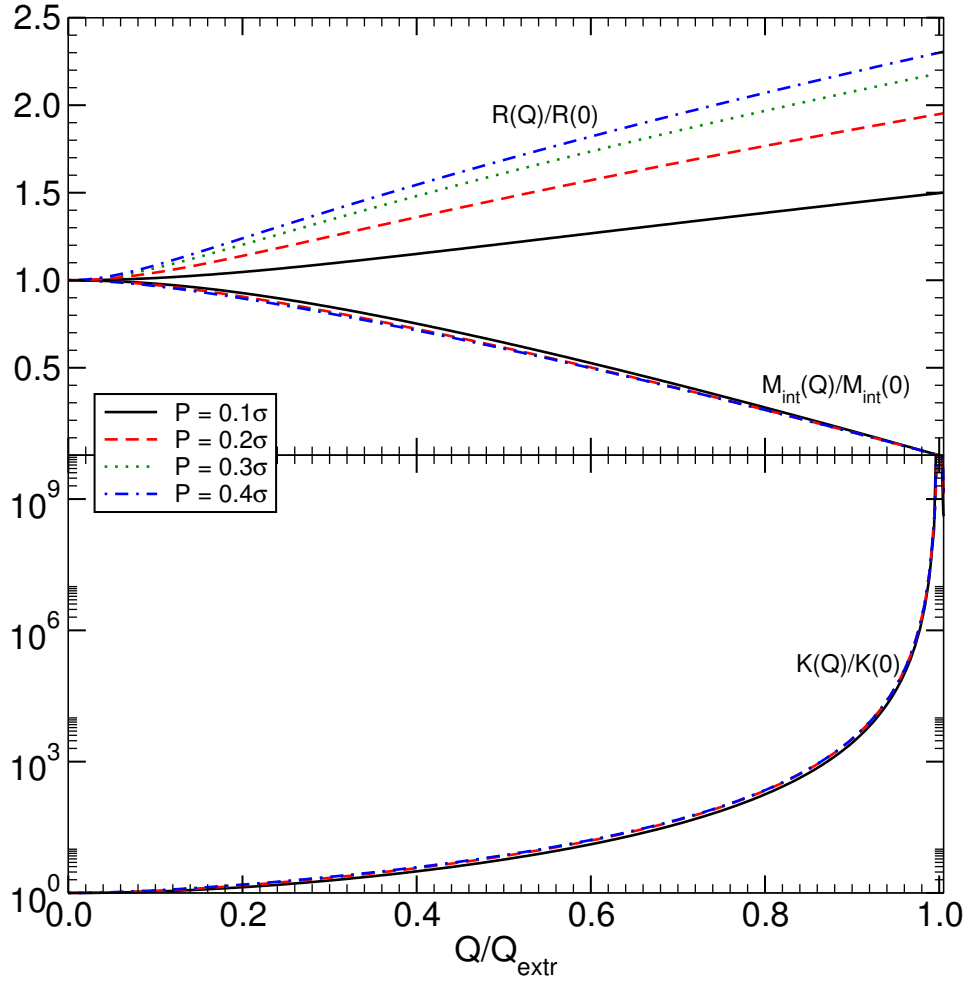
Figure 4.4: Hairy solutions. The position R of the matter distribution, the internal mass M_{int} and the curvature scalar K are shown as function of the scalar charge Q for different values of the pressure P. The surface energy density is set to $\sigma M = 10^{-3}$.

Results: hairy solutions

The results are summarise in figure 4.4: the plot is unique because the exact solutions agree very well with the perturbative ones, even if the latest are considered up to the first order in Q.

We numerically integrate for the scalar charge Q the exact field equations (4.23) and (4.24) keeping the total mass M fixed. In figure 4.4 we show the internal mass M_{int} from equation (4.31), the shell position R and the Kretschmann scalar $K = R_{abcd}R^{abcd}$ at the black hole radius r_h as functions of Q.

In the plot, we normalise all quantities by their general relativistic values, i.e. the $Q = 0$ case, and the horizontal axis has been rescaled by Q_{extr}, which corresponds to the extremal solution such that $M_{\text{int}}(Q_{\text{extr}}) = 0$, i.e. no black hole at all. With these normalisations, the quantities M_{int} and K are almost universal for different values of the pressure. K in a scalar invariant that gives us information on the curvature; indeed in the limit case of $Q = Q_{\text{extr}}$, K diverges since the disappearance of the black hole (i.e. of its horizon) leaves the singularity *naked*. As the charge increases $Q \to Q_{\text{extr}}$, the internal mass decreases and the shell is pushed further away, i.e. R increases.

Concluding: for large values of Q, the structure of the hairy black hole can be very different from its general relativistic counterpart. We have thus constructed **nonlinear, hairy solutions of scalar-tensor theories with a black hole at the centre**, and since they are the only static spherically symmetric solutions to the field equations, we claim they are the end state of the instability that the matter profile has triggered in the Schwarzschild background metric.

We found an infinite number of hairy solutions, depending only on the parameter Q, i.e. on the constant value of the scalar field in the interior. On the other hand, in the case of spontaneous scalarization in neutron stars Q assumes only specific values (Damour and Esposito-Farese, 1993, 1996; Pani et al., 2011). This is probably due to our assumption that the matter distribution does not have a back reaction in the metric (i.e. the metric in the interior is Schwarzschild), otherwise the asymptotic behaviour of the scalar field is determined by the matter configuration near the black hole and one expects that regular solutions (at the horizon and at infinity) would sort out only a finite number of scalarized configurations.

Chapter 5

The restless dark matter

As we already discussed in chapter 1, observations suggest that structure formation in the Universe proceeds hierarchically, with the smallest structures collapsing first and then later merge to form lager structures.

When a small structure is engulfed by a larger one, it will be ripped apart dynamically and a new equilibrium state will be eventually reached. At the end of this relaxation process, the virial theorem must hold

$$2K + W = 0 \,, \tag{5.1}$$

where K and W are the total kinetic and potential energies of the system.

Let us consider a merger between two structures. Initially they are singularly in steady state, so the virial equation holds for both

$$2K_1 + W_1 = 0 \,, \qquad 2K_2 + W_2 = 0 \,.$$

If structure 1 is much bigger than structure 2, i.e. $W_1 \ll W_2$, then the initial energy of the big is $E_1 = K_1 + W_1 = -K_1$, whereas we can ignore the potential in the total energy of the small when we consider the merger, so $E_2 = K_2$. When equilibrium is reached again, the new structure has a final kinetic energy K that has to satisfy the virial theorem:

$$K = -E = -(E_1 + E_2) = -(-K_1 + K_2) = K_1 - K_2 \,.$$

Thus, equilibrium after a merger doesn't come for free, but an amount of energy of roughly $2K_2$ has to be disposed. Baryons can easily radiate away this energy, cooling down and reaching the so called virial temperature. However, if we are dealing with dark matter, which is non-radiative, the halo can reach a virial equilibrium without any signification modification of the large structure by ejecting some particles out of the system and let them carry the energy that has to be discarded.

On energetic grounds, it is thus clear why particles ejections are experienced in the course of mergers.

The relaxation and mixing processes in collisionless mergers have been examined in (Valluri et al., 2007), where they found that mixing of the 6-dimensional phase space distribution function mainly occurs during the tidal shocking arising when the centre of the merging halos pass through each other. They also find that around 40% of the particles from the merging halos are located outside the virial radius of the remnant. In controlled numerical galaxy collisions it has been known for years that some particles are ejected with positive energies, e.g. in (Hernquist, 1990). In cosmological simulations (i.e. within an expanding background) it has been found that unbound particles are abundant in halos which have recently undergone a major merger (Behroozi et al., 2013).

Our goal is to understand the mechanism responsible for the ejection: how do particles acquire energy enough to leave the system in which they are bound? How are the *sacrificed* particles different from the others?

These are the questions we address by performing numerical simulations.

Chapter 6

N-body simulations

The physical processes involved during mergers are hard to quantify due to the rapidity of how the two encounters reach a new steady state: few crossing times. This highlights the need of using numerical simulations rather than analytical arguments as first approach towards an understanding of the phenomenon.

We investigate dark matter halo mergers through N-body simulations. We observe an ejection of particles initially belonging to the smaller halo as consequence of the relaxation of the resulting structure. We focus on the features of the ejection.

6.1 Simulations Set-Up

Our aim is to study systems with extremely large number of particles as dark matter halos. Among these particles the only force acting is gravity, which is a long-range interaction. In this kind of configurations, the two-particle relaxation time greatly exceeds the age of the structure: **the system is collisionless**. We perform three-dimensional simulations using GADGET-2 (Springel, 2005), a massively-parallel N-body code. We are interested in the dynamics intrinsic to the system, thus we do not need to consider a cosmological background: the space is not expanding and the gravitational potential Φ computed is purely newtonian

$$\Phi(\vec{x}) = -G \sum_{i=1}^{N} \frac{m}{|\vec{x} - \vec{x}_i|} \, ,\tag{6.1}$$

where N is the total number of particles and m their mass, $\vec{x}_i$ their position in space.

We use natural units, setting the gravitational constant G to unity. In equation (6.1)

We mimic a merger between two dark matter halos by tracking the trajectories of $1.1 \cdot 10^4$ particles, 10^4 belonging to a halo and 10^3 to a smaller

one. We set the mass-ratio of the halos to $1 : 10$, thus all particles have the same mass.

In GADGET-2 all the two-body interactions are calculated assuming point-like particles; in order to speed up the computation, to calculate the force acting on each single body the software separates the rapidly varying forces due to the small number of nearby particles from the slowly varying forces due to the large number of distant ones using a so called tree-code. Numerical infinities can arise when the distance between two particles $|\vec{x}_j - \vec{x}_i|$ becomes tiny. To avoid them, the code adopts a different spline for distances shorter than a specified softening length ϵ. We estimated ϵ to be of the order of the mean inter-particle distance of our structure $\epsilon \sim m^{1/3}$, so we set $\epsilon = 0.046$. We check whether our choice doesn't introduce relevant errors in the computation of the gravitational force using the constancy of the total energy of the system as a proxy.

6.1.1 Initial conditions

At $t = 0$ the particles are grouped into the two halos. The positions and the velocities of the particles are chosen so that each structure, treated as an isolated system, is in a steady state. Positions are assigned from the Hernquist density profile (Hernquist, 1990), with constants ρ_0 and r_s

$$\rho(r) = \frac{1}{r/r_s} \frac{\rho_0}{(1 + r/r_s)^3} \, , \tag{6.2}$$

and the velocities from a Gaussian probability distribution function with the initial isotropic velocity dispersion derived from the Jeans equation (Binney and Tremaine, 2008). All initial velocities are truncated at $0.95 \, v_{esc}$, with v_{esc} the escape velocity of each halo.

The constant ρ_0 in equation (6.2) is such that the two halos have masses $M_1 = 1$ and $M_2 = 0.1$; we run different simulations keeping the scale radius of the big halo fixed $r_{s1} = 1$ and varying the small halo one within the range $0.1 \leq r_{s2} \leq 0.7$, corresponding to denser to more diluted structures.

The centres of mass of two halos are placed at $y = 0$ and $z = 0$ in our cartesian coordinate system. Instead in the x direction we set the major halo at 0 and the minor at 15. The latter value is a rough calculation of the turnaround radius of the big structure (Prada et al., 2006; Cuesta et al., 2008), assuming it has a typical concentration of galaxies (Maccio' et al., 2008). The turnaround radius corresponds to the the distance a particle can reach before being gravitationally pulled back towards the centre of its belonging structure in an expanding universe, thus catching the moment in which the particle's velocity is zero before inverting sign. The choice of placing the small halo at the turnaround radius of the big one allows us to let the simulation start with the centres of mass of both halos at rest. Then the minor structure starts approaching the major one, pulled by gravitational
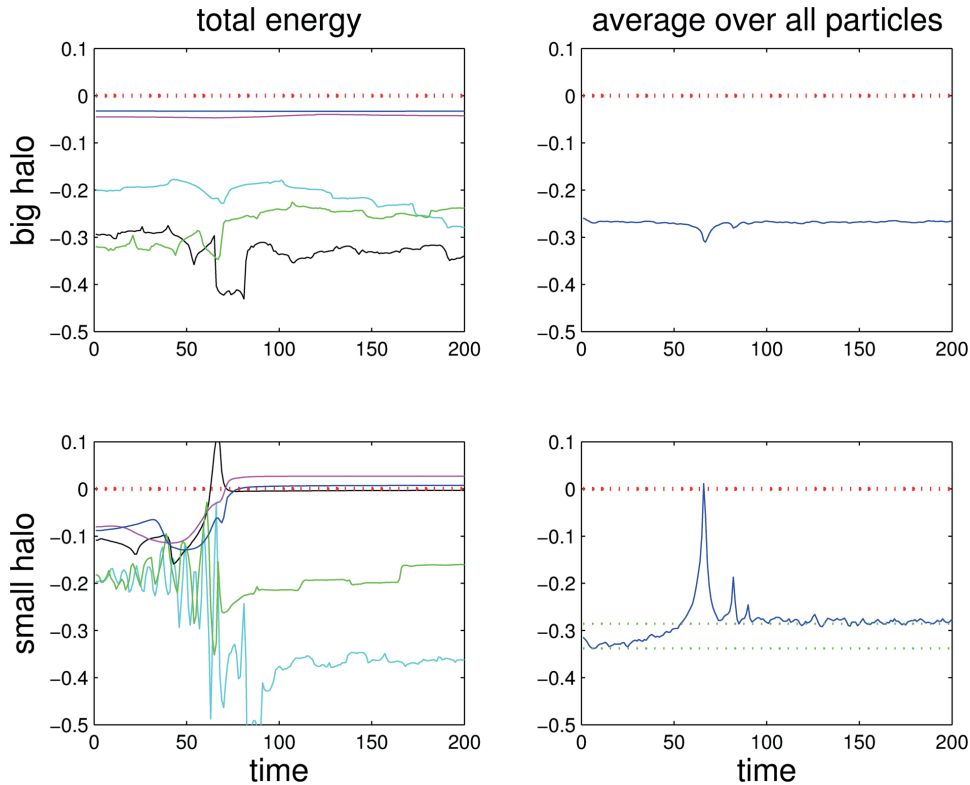
Figure 6.1: Time evolution of the total energy. On the left relative to 5 random selected particles, on the right the average over all particles. Top is for the major halo, bottom for the minor. The red dotted line corresponds to the zero point of the energy.

attraction. After the merger, we continue the simulation for at least 10 more dynamical times, where we define a typical dynamical time τ_{dyn} from the circular velocity v_c at $r_4 = 4\,r_{s1}$, $\tau_{\mathrm{dyn}} = r_4/v_c(r_4)$.

By checking whether the total energy of the resulting structure without the ejected particles reaches a constant value, we assure the system reaches a new equilibrium.

We then run a test simulation increasing the number of particles by a factor of 10 for both halos and reducing the softening length ϵ by a factor of 2 confirming our findings.

6.2 Results

6.2.1 A first simulation

We first run a simulation with $r_{s2} = 0.3$.

For a particle to be ejected, i.e. not bounded anymore, it needs to acquire
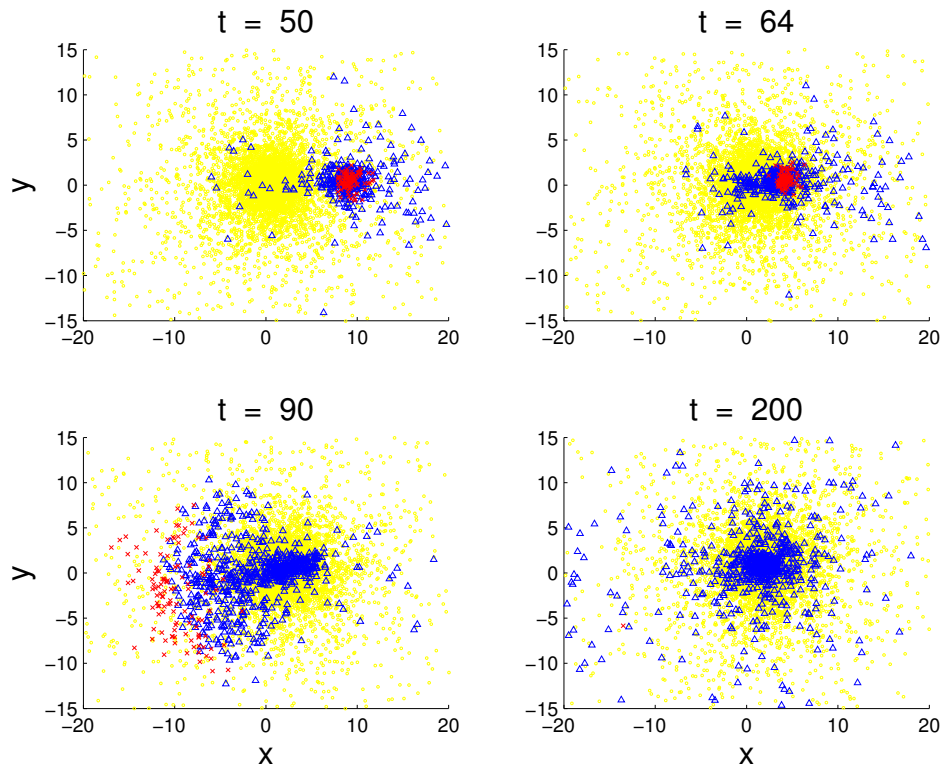
43

Figure 6.2: $r_{s2} = 0.3$ simulation. The positions in the x and y directions of the particles at different time steps. The yellow dots belong to the major halo, the blue triangles are minor halo particles that stay bounded throughout the run, the red stars are minor halo particles that get ejected.

positive total energy. To check if we experience ejection of particles when a merger takes place, we analyse the energy time evolution of all particles in the simulation. For example, in figure 6.1 we plot the energy of few randomly selected particles. In the case of the big structure, its particles' energies never leave the negative area of the plot, they stay roughly constant in a range of values well represented by the total mechanical energy of the halo averaged over the number of its particles.

Among the chosen particles belonging to the small halo, there are a couple for which the mechanical energy becomes positive after the merger, happening roughly during the time steps $60 \div 70$. The mean particle energy of the small halo displays a sharp peak at the moment of the merger and than falls back to a roughly constant value, which is higher than the initial one.

We identify the **ejected particles** as the ones with a total energy greater than zero at the last time-step of the simulation. After having spotted them, we can follow their trajectories from the beginning of the run. We do so in figure 6.2, where we plot the position of the particles in the (x, y) plane at different time steps, with the red stars indicating the particles ejected after the merge.

The colour code allows us to follow the ejected particles in red from the beginning of the run, to distinguish them from the other particles belonging initially to the small structure, in blue, and those belonging to the big structure, in yellow. We see that at $t = 50$ the small halo hasn't yet crossed the big halo core and the red particles are well mixed with the blue ones. As the small halo enters the large halo's core at $t = 64$, we see that the red particles are those which "lag behind" and are the last ones to cross the core. The next snapshot describes the subsequent ejection, and in the last one at $t = 200$ (~ 23 dynamical times of the big structure τ_{dyn}) there are no longer red particles within 15 times the scale radius r_{s1}, thus confirming our predictions about the discharge of particles.

During a collision, some particles are freed from the system and will never return, as happens to the 11% of the minor halo ones in this simulation, whether no large halo particle is ejected.

None of the particles are freed before $t = 50$, so it is probably the merger the cause of the ejection.

6.2.2 The ejection mechanism

Having identified all the ejected particles, we can plot the comprehensive energy behaviour of the latest and compare it with that of the particles that never leave the structure, as in figure 6.3. In the bottom panel we show the potential energy behaviour and we see clearly that on average the escaping particles (red) fall in the resulting potential well slightly later than the bounded (blue) ones. Moreover, going back to the $t = 64$ plot in
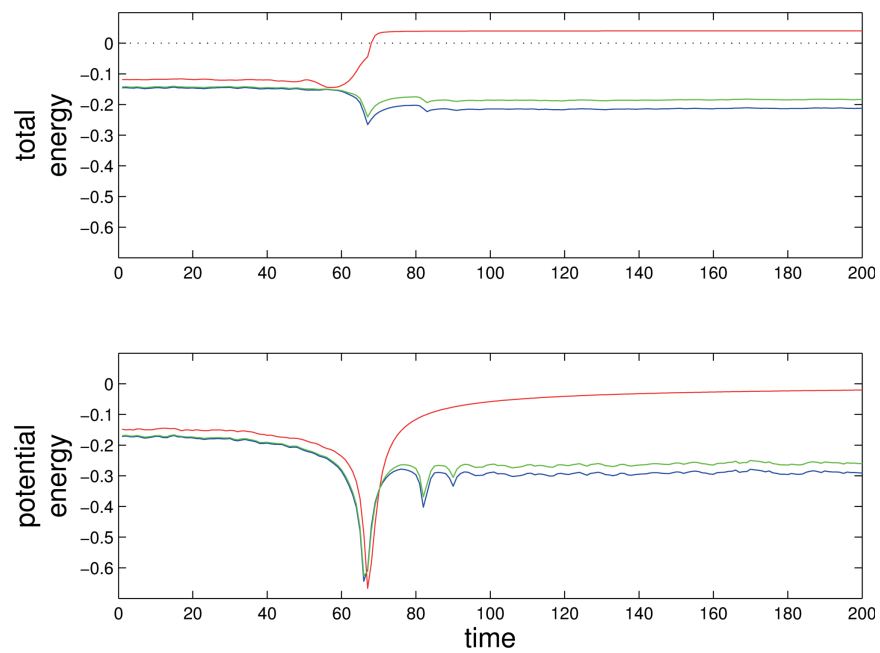
Figure 6.3: Time evolution of the total (upper plot) and potential energies (bottom plot) averaged over the number of particles of the whole small halo (green), of the particles that stays bounded (blue) and of the ejected ones (red).
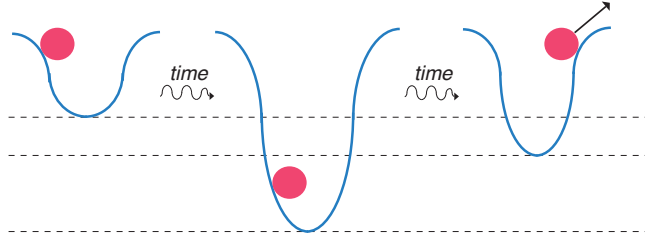
Figure 6.4: An illustration of the potential well during the merger. The red ball corresponds to a particle that will later be ejected.

figure 6.2 (top right panel), we notice that all the ejected particles (red) are on the *right side* of the minor halo when the two cores start blending.

Combining these two evidences, we get the picture that the particles that just happen to arrive later in the region at the centre of the merger pick up a large positive kick to their energy in a short time as they pass through the time-dependent potential well created by the rest of the mass, as shown in the diagram 6.4; the abrupt change in potential when the particles are passing through it give them enough energy to reach and to exceed the escape velocity of the structure.

In the mechanism of ejection we recognise that of violent relaxation as originally described by (Lynden-Bell, 1967) for stellar systems: starting from an initial configuration which is far from dynamical equilibrium, such a system can relax precisely because, in the time dependent gravitational potential, particles' energies can change rapidly (i.e. on mean field time scales). It is a matter of how violent the potential fluctuations are for the ejection to take place.

A detailed view of the time evolution of particles' energies here reveals that what is happening in the minor merger is very similar. In figure 6.5 we zoom in on the time steps during the merger. For simplicity, we pick again 4 random selected particles and we follow their energy evolution, where the green and red (dashed lines) are ejected particles, whereas the black and purple (dotted lines) stay bounded. We also show the energy of the most bound particle from the small structure (stars), and the same from the big structure (triangles). Inspecting the time steps between 62 and 67, we see that the potentials of both the small and the large structures get deeper. This is naturally because during the first passage when the two structures overlap for the first time, the potentials deepen. However, during the time-steps from 67 to 70 the potential falls back to a smaller absolute value. This is just after the first passage of the small structure. After this point, the potential flattens out close to the final value.
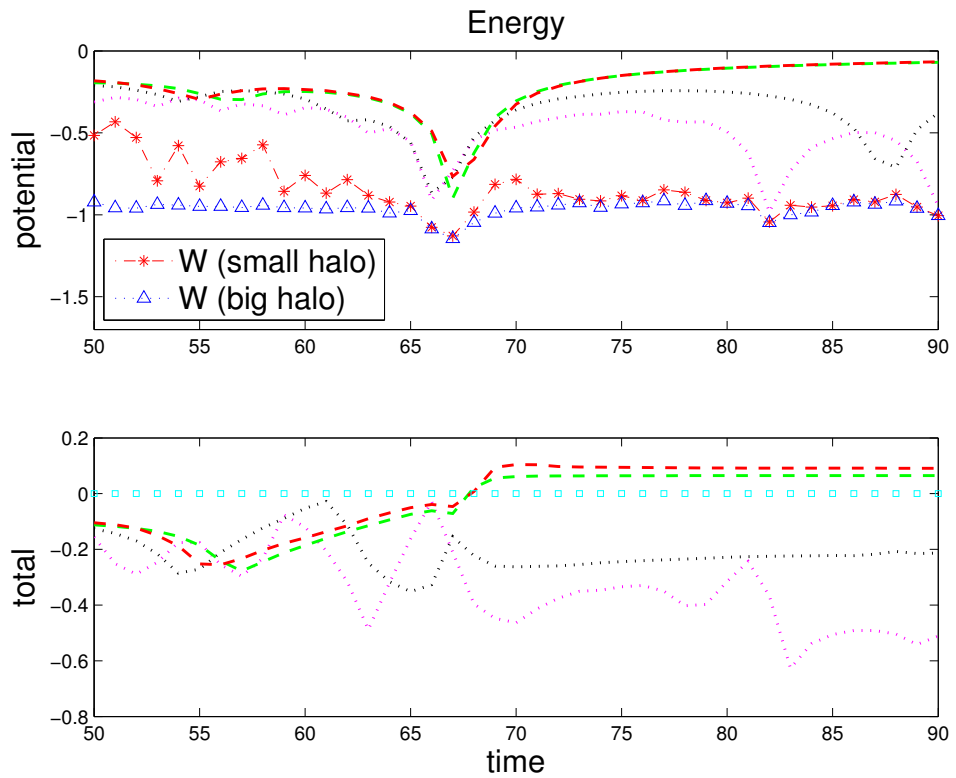
47

Figure 6.5: Time variation of potential and total energies of some sampled particles. The ones which will remain bound (black and purple dotted lines) pass through the central region while the potentials due to both the small and large structures (symbols) are deepening (around time step 66). This contrast with the particles which will be ejected (red and green dashed lines), which arrive a little later (time step 67) and pass the centre when the potential is growing.
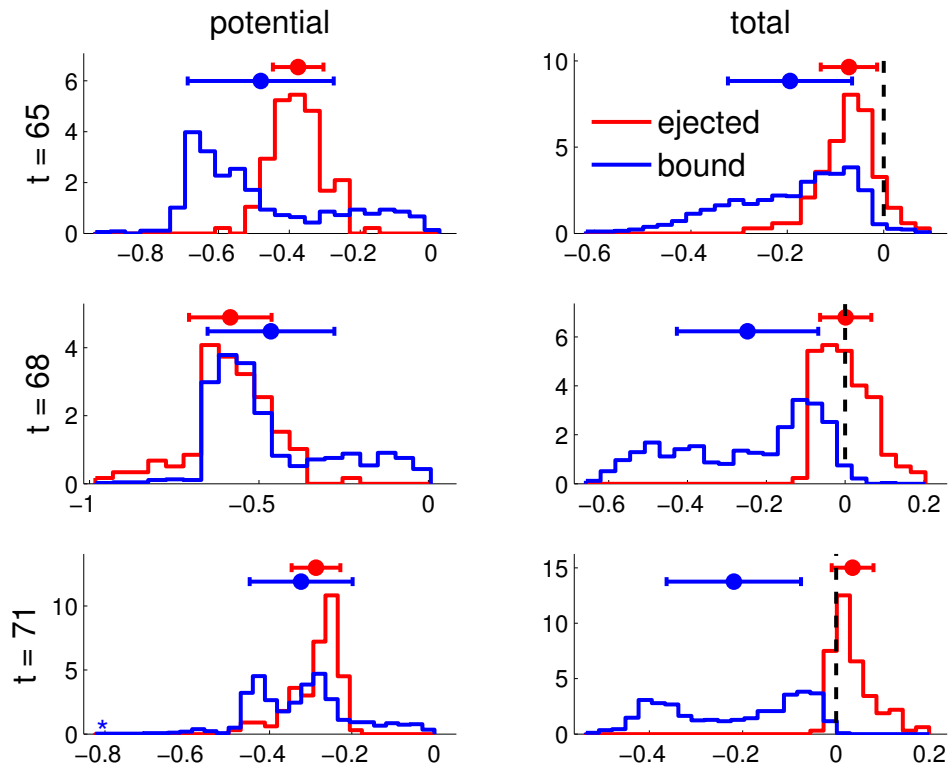
Figure 6.6: The potential (left) and total (right) energies distributions for the ejected particles (red) and for the remaining minor halo particles (blue) at different time steps. Above each distribution, we indicate the mean value (dot) and the standard deviation (bar). In the total energy plots, the dashed black line signals the zero value.

Now, comparing the time of passage of the particles which will remain bounded (black and purple dots), we see that they pass the centre during the deepening of the potential of the structure. On the other hand, the particles which are ejected arrive later during the phase when the potential happens to be weakening (i.e. increasing towards less negative values). As the sign of the time derivative of the mean field potential is positive, the energy of the particles increases, since the time variation in particle's energy along a trajectory is equal to the time derivative of the potential energy, according to the relation (Lynden-Bell, 1967):

$$\frac{dE}{dt} = \frac{\partial W}{\partial t} \ .$$ (6.3)

To stress that the *late arrival* of the ejected particles is statistically founded, in figure 6.6 we plot the potential energy distribution among the ejected particles (red) and among the rest (blue), for the crucial time steps of the merger. At $t = 65$ the red particles are indeed characterised by a higher potential values while the blue are deepening the potential; at $t = 68$ there is the shift: the red particles reach the bottom of the potential when the blue ones are already gaining potential energy, thus inverting the potential time derivative (the number of blue particles is ~ 10 times bigger than the red); finally, at $t = 71$, the red particles are again the ones less bound, indeed the ejection has started since, from the total energy distribution on the right plot, we notice that the red mean total energy is already positive.

We note that this effect is analogous to the so-called late-time integrated Sachs-Wolfe effect, in which CMB photons gain energy because of the alike wells and hills of the potential they are traversing.

6.2.3   Which particles are ejected?

The observation that it is the particles coming in later which are ejected is similar to the case of cold uniform spherical collapse in (Joyce et al., 2009), where the ejected particles are found to be those starting out in the outer shells. In this case, close analysis of the particles' energies shows that those which escape pick up the energy leading to their ejection when they pass through the potential generated by the bulk of the mass which has already turned around and started re-expanding: as the time derivative of the potential energy $\partial W/\partial t$ is then positive, they gain energy E, as in equation (6.3).

To check if also in our case is the initial position of the particles to be relevant, in figure 6.7 we plot the radial velocities and the radii of the small structure particles before the merger happens, for three different values of r_{s2}. With red circles we refer to the particles that are later ejected. They are evenly distributed among all particles, in the sense that at any given radius the velocity distribution of the particles which are subsequently ejected is
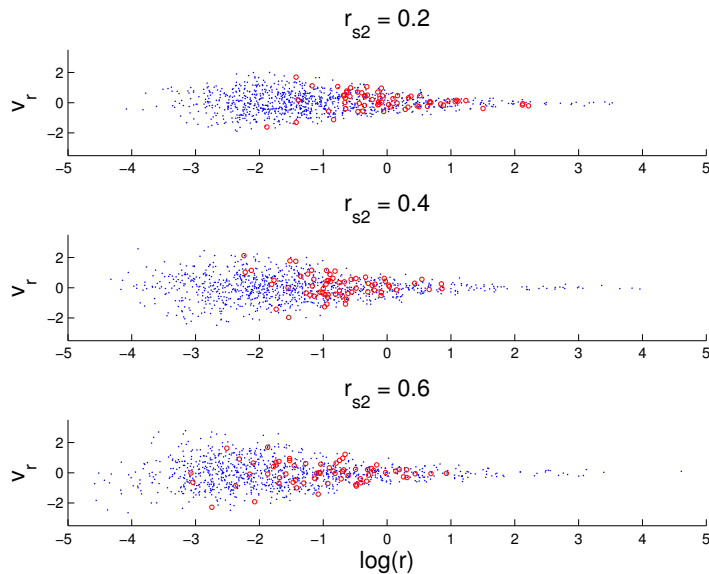
Figure 6.7: Logarithm of the radius r and radial velocity v_r normalised with the related virial quantities for 3 different scale radius minor halos particles before the merger takes place in every different simulation. The red circles represent the particles which will be later ejected, the blue dots the particles which remain bound.

similar to that of the particles which remain bound: they are not either the most energetic or the furthest from the centre of the halo.

Also when plotting other quantities as the angular momentum (its module and its direction) we cannot find any particular feature that characterised the particles in question. Thus, the decisive factor seems to be whether or not a particle is falling early or late into the combined potential of the cores of the halos.

6.2.4 The fraction of ejected particles

We run different simulations changing the size of the minor halo (varying r_{s2}) to check how this affects quantitatively the ejection. In figure 6.8 we plot the behaviour of the ejected particles fraction f^p as function of the dynamical time for 11 different simulations. f^p is the ratio of the number of ejected over the total number of particles initially belonging to the minor halo. The number of ejected particles grows up to a peak that corresponds roughly to a small structure with a dynamical time $\tau_{\rm dyn}(minor) \simeq 0.7\,\tau_{\rm dyn}(major)$, then the number starts decreasing monotonically.

We are able to interpret this behaviour thanks to the considerations made in the previous section. We are comparing two timescales, namely the time it takes the small structure to cross the big structure, and the time for
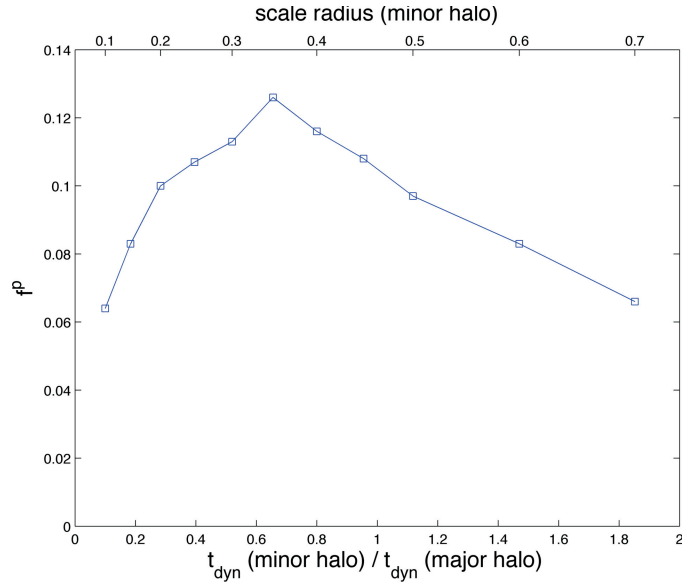
Figure 6.8: The value reached by the fraction of ejected particles f^p after the merge as function of the dynamical time (and scale radius) of the small halo in each simulation, normalised with that of the big halo.

a typical orbit in the small structure. The first timescale corresponds to the crossing time for the big structure, which is proportional to our definition of the dynamical time, $\tau_{\mathrm{dyn}}(major) = 4r_s/v_c(4r_s)$. The second timescale is similar, but defined for the small structure, $\tau_{\mathrm{dyn}}(minor)$. Thus, in a very compact small structure (low values of r_{s2}), its particles make many orbits while crossing the big structure, and fewer receive sufficient increase in energy to leave the structure. On the other hand, in a very dilute small structure (high values of r_{s2}), the particles perform much less than one orbit while crossing the big structure, rendering the motion almost adiabatic.

An extrapolation of the last statement is that smooth accretion should not lead to particle ejection.

The outcomes of the N-body simulations point out that the mechanism behind the particle ejection is a mean-field effect.

Chapter 7

Simulations with analytical potentials

In order to demonstrate that the ejection of particles during mergers is a mean field effect, we implement a toy-model in which we consider one particle moving in an analytical time-dependent potential. In this way we eliminate all two-body interactions that could affect the motion of the test particle.

7.1   Simulation Set-Up

Since we want to test the conclusions reached analysing the N-body simulations, we set up a new kind of 3-dimensional simulations using the same parameters, to make the results of the two different experiences comparable.

We consider three bodies: two structures and one single particle. The two structures are described by their analytical potential Φ correspondent to a Hernquist halo (Hernquist, 1990)

$$\Phi(r) = -\frac{M}{r + r_s} \,. \tag{7.1}$$

The major halo has mass $M_1 = 1$ and scale radius $r_{s1} = 1$ and for the minor halo $M_2 = 0.1$, as in all N-body simulations. We pick $r_{s2} = 0.3$ as small structure scale radius, since it is the case we refer the most also in chapter 6.

For simplicity, the larger structure stays still during the whole simulation, the smallest moves accordingly to the gravitational attraction of the other. The particle feels attraction from both structures and we follow its orbit and energy.

Initial conditions

Initially the centre of mass of the small halo is placed at the origin of our (x, y, z) coordinate system, the big one is at $(15r_{s1}, 0, 0)$, where $15r_{s1}$ is the values of the turnaround radius described in section 6.1.1 that allows us to let the minor halo start from rest.

The protagonist particle of the experience is initially bound to the small structure. Its initial position and velocity are different every time the simulation runs. First we randomly choose a radius using the Hernquist mass profile

$$M(r) = M_2 \left(\frac{r}{r_{s2} + r} \right)^2 , \tag{7.2}$$

i.e. we pick a random number α using the normal distribution, than the chosen radius $\bar{r}$ is such that

$$M(\bar{r}) = M_2 \cdot \alpha ,$$

with cutoff at $r_{max} = 1$. Also the angles are randomly built from α and we finally set the initial (x, y, z) of the particle. The initial velocity is chosen in a similar way, determining a typical speed $\bar{v}$ at the radius $\bar{r}$ just found. We use the analytical expression for the isotropic velocity dispersion $\sigma^2(r)$ (Binney and Tremaine, 2008)

$$\sigma^2(r) = \frac{1}{\rho(r)} \int_r^\infty \frac{\rho(t) \, M(t)}{t^2} dt , \tag{7.3}$$

where the expressions for the density ρ and mass M are in equations (6.2) and (7.2). We take the speed $\bar{v}$ such that

$$\bar{v} = \sqrt{\frac{\sigma^2(\bar{r})}{3}} ,$$

from which we randomly derive the initial velocity components (v_x, v_y, v_z).

Numerical integration

We run simulations from $t = 0$ to $t = 100$, with a typical time step of $\Delta t = 0.005$. For each time step i we update positions and velocities of the two moving objects (minor potential an particle) using a leapfrog integrator, i.e. in the three different spatial directions

$$\begin{aligned}
x_i &= x_{i-1} + v_{i-1/2}\Delta t , \\
a_i &= F(x_i) , \\
v_{i+1/2} &= v_{i-1/2} + a_i \Delta t ,
\end{aligned}$$

where F is the Newtonian gravitational force respectively acting on

- the small halo, due to the big one,

- the particle, due to both halos.

Since the two structures are aligned in the x-direction, the minor one moves along this coordinate. Also the particle bound to the small halo follows this x-motion, at the same time keeping orbiting around the structure. We check its motion by looking at its total energy (with the kinetic one calculated with respect to the small halo) which remains constant up to when the merger takes place.

Once the minor halo centre of mass reaches the major one, we arrange different scenarios trying to cover all possible situations among which any realistic N-body simulation would lie:

case 1: the minor halo stops, we let only the particle keep moving,

case 2: the minor halo doesn't stop and keeps moving in x still in free fall, accordingly slowing down,

case 3: the minor halo stops as in case 1 and the merger has a small impact parameter,

case 4: the minor halo doesn't stop as in case 2 and the merger has a small impact parameter.

Since in a realistic situation the small halo is engulfed by the big one, the two extremal situations (small halo totally stops or goes on unperturbed) span the real outcomes of the phenomenon and thus can be confronted with the N-body simulations' results. The two cases involving an impact parameter are complementary to the N-body simulations already performed: in that experience we run only head-on mergers, therefore we check how much the problem changes with this slightly different setup.

To mimic the presence of an impact parameter, we forcedly change the velocity of the small halo in direction $v_x \longleftrightarrow v_y$ when the its centre is at $x = 5$ for few ($\sim 10^2$) time steps (this number fairly changes randomly to perform different impact parameters each run).

7.2   Results

The goal of this experience is to check what happens to the particle after the merger between the two analytical potentials: does it stay bound to the minor halo, gets trapped by the major halo or is ejected from the system?

In figures 7.1 to 7.4 we summarise the different outcomes of the runs. We plot the positions of the centre of the two potentials and the orbits of particles of different simulations for each case in the (x, y) plane.
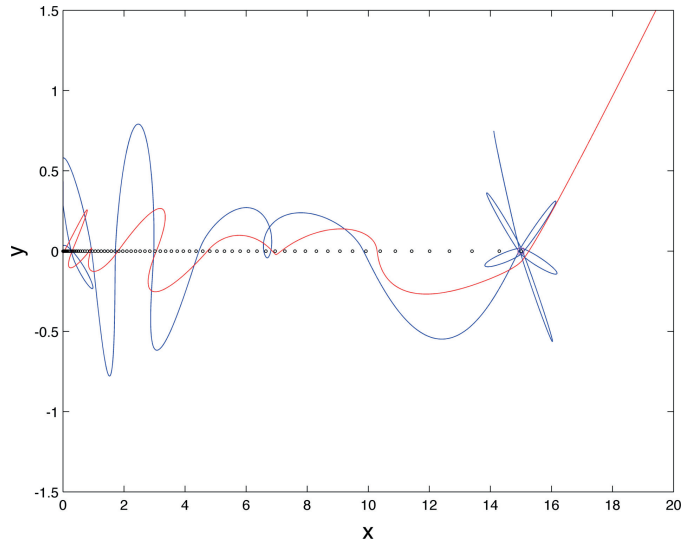
Figure 7.1: **Case 1.** (x,y) plane. The minor potential (black dots at equal time intervals) stops as it overlaps the major potential (magenta square at (15,0)). The particle with the blu orbit stays bound in the resulting structure, the red runs away from the system.

In cases 2 and 4 the particle can also get trapped by the big potential, as it happens to the green orbits in figures 7.2 and 7.4. In all cases, the particle can be kicked away (red orbits) or stays bound to the small potential or in the resulting structure (blu orbits).

To check which one of the three possible final states characterises the particles of each different run, we control the sign and constancy of their total energies. We show for example in figure 7.5 the energy time evolution for an ejected (in red) and bound (in blue) particles belonging to two case 2 simulations. We see that before the merger takes place ($\sim$ at $t = 72$) both particles are bound, their total energies are constant and the kinetic and potential one oscillating complementarily. At the merger time they experience an abrupt fall in potential energy, then the blue particle energies start again oscillating although differently, meanwhile the red particle kinetic energy steadily increases, the potential approaches zero and the total energy gets greater then zero, i.e. the particle is out of the system.

To get enough statistics we run the code 4000 times, 1000 simulations for each of the 4 cases. In table 7.1 we show the results.

For the N-body simulation with the same parameters we used in these runs, the fraction of ejected particles is 11%, which lies between the values of the head-on runs, cases 1 and 2, respectively 14% and 5.3%.

We notice that for non head-on simulations the ejection probability increases by few percentage points.
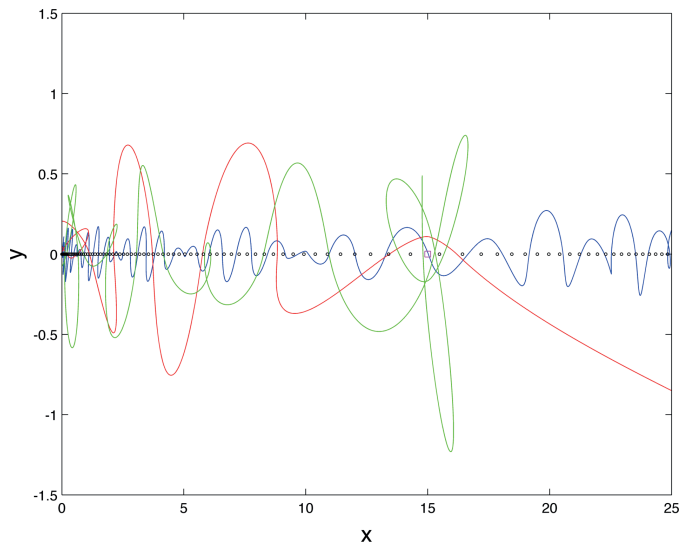
Figure 7.2: **Case 2.** (x,y) plane. The minor potential (black dots at equal time intervals) is in free fall motion, the major potential stays still (magenta square at (15,0)). The particle with the green orbit gets trapped by the major potential, the red runs away from the system and the blu stays bound in the minor potential after the merge.
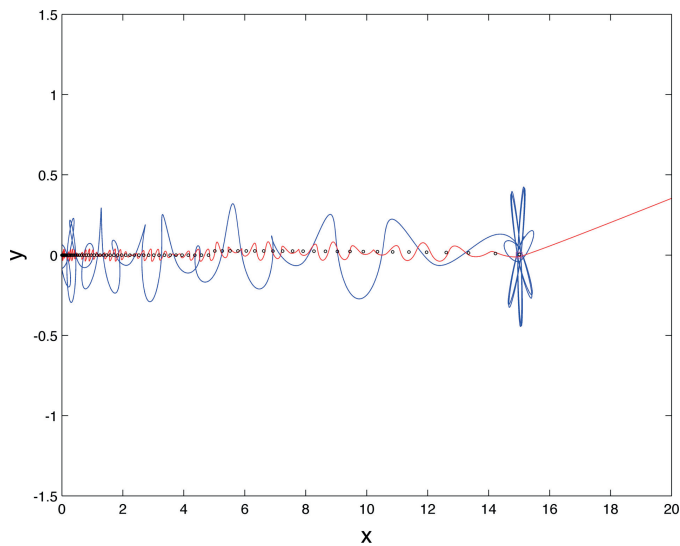
Figure 7.3: **Case 3.** (x,y) plane. The minor potential (black dots at equal time intervals) approaches the major potential (magenta square at (15,0)) with an impact parameter and stops as the two centres of mass overlap. The particle with the blu orbit stays bound in the resulting structure, the red runs away from the system.

Figure 7.4: **Case 4.** (x,y) plane. The minor potential (black dots at equal time intervals) is in free fall motion and approaches the major (magenta square at (15,0)) with an impact parameter. The particle with the green orbit gets trapped by the major potential, the red runs away from the system and the blu stays bound in the minor potential after the merge.
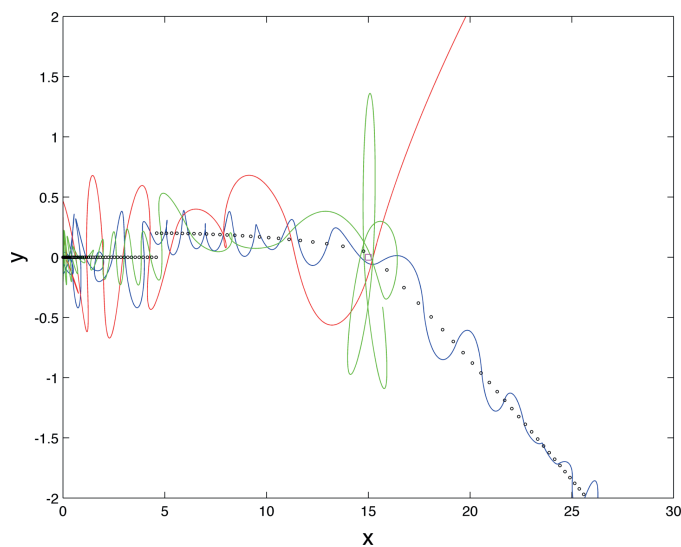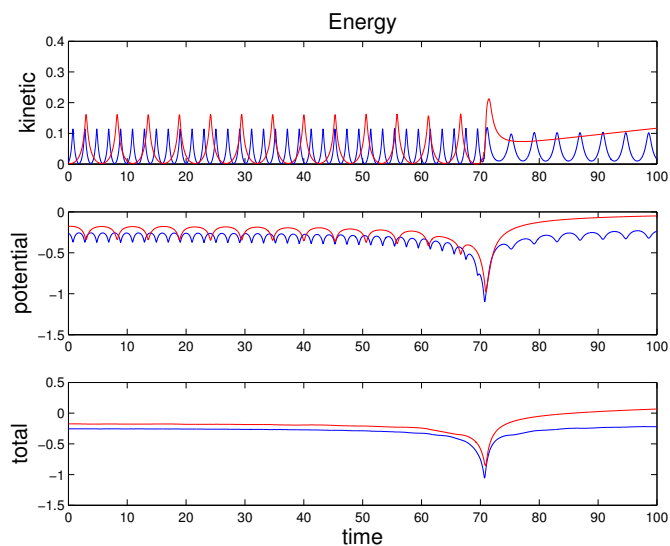

Figure 7.5: **Case 2.** Time evolution of the energy of a particle that stays bound (blue) and of an ejected one (red). Top plot is the kinetic to respect of the small halo, middle plot for the potential and in the bottom the sum of the two above.

Table 7.1: **Ejection statistics.** 1000 simulations run for each case. In cases 2 and 4 the small halo keeps moving and the particle can also get trapped by the big halo, otherwise, as in the other two cases, it can get either ejected or can stay in the small halo.

	Ejected	Small halo	Big halo
Case 1 Halo stops. Head-on.	14%	86%	
Case 2 Halo doesn't stop. Head-on.	5.3%	82.4%	12.3%
Case 3 Halo stops. Impact parameter.	17%	83%	
Case 4 Halo doesn't stop. Impact parameter.	7.2%	76.7%	16.1%

Chapter 8

Conclusions

The first part of this work was dedicated to the study of black holes in scalar-tensor theories of gravity with a surrounding mass distribution. We have demonstrated that two different kinds of instabilities can arise, depending on the sign of the effective mass squared μ_s^2 that shows up coupling the theory to matter.

When μ_s^2 is positive and the black hole is rotating superradiance is triggered, when it is negative and there is sufficient matter the initial general relativistic solution can develop scalar hairs, undergoing an effect called spontaneous scalarization. The efficiency of the instability depends on the matter profile, the hole's rotational velocity and the considered scalar-tensor theory. Moreover, superradiance is also responsible for the existence of long-living modes propagating on the black hole background, that can be amplified with gain factors up to 10^5.

Our discussion has been especially qualitative. Having at our disposal a more realistic framework, these effects could lead to **constraints on the parameter space of scalar-tensor theories**. This would involve a non linear time evolution analysis of the instabilities, to understand the dynamical development and the final states, and the improvement of the mass profile we consider (e.g. modelling an accretion disk, which is not spherically symmetric). Regarding the last point on spherical symmetry: thinking of the superradiant case, it could be argued that a more realistic geometry of the problem could kill the instability (i.e. would be easier for the modes to escape and not be reflected if we had a disk and not a sphere trapping them), but it should also be taken into account that we expect matter to be rotating at high velocity around the black hole: what would be the effect of rotation on the reflectivity of the mass distribution inner surface? Addressing this question could be a possible spinoff of this work.

Moving on to the observational imprints our results could have, we expect the nontrivial scalar profile developed by spontaneous scalarization to affect the inertia moment of **binary systems** and the production of **grav-**

itational waves (e.g. what has already been studied within neutron stars, see (Damour and Esposito-Farese, 1996; Barausse et al., 2012)).

Instead, superradiance slows down the **black hole rotation**. This could be directly observed (e.g. recently X-ray spectroscopy has improved spin estimations, see (Reynolds, 2013)) or we could speculate that different black holes at different redshift should follow a rotational velocity trend: the younger (closer) ones spinning faster then the older (further).

Concluding, thanks to their simplicity, black holes are considered the most viable way to study gravity in strong regime and also high energy physics in some cases, with more convincing results coming up also from the observational side, as recently reviewed in (Cardoso, 2013), so the techniques used in this work could serve in other on-going topics.

In the second part of thesis, we have looked at the mechanism of particle ejection that follows dark matter halo mergers.

We have shown that during mergers approximately $5 - 15\%$ of the particles from the minor halo are ejected. We have demonstrated that this ejection is a mean field effect, with the increase in the total energy of individual particles arising from the time-dependence of the mean field potential during the merger process. Our results also leads us to expect that particles should not be ejected during smooth accretion.

Our finding provides an explanation for the **origin of high-velocity component of dark matter particles** observed in cosmological N-body simulations. This component of high-velocity particles is important since it potentially may give a clear signature in underground **dark matter detectors** (Behroozi et al., 2013). This is because particles ejected from other merging structures may be passing through the Milky Way at energies significantly higher than the equilibrated dark matter component of our galaxy.

Moreover, these results should be taken into account in determining the **distribution functions of merger remnants** (dark matter halos or galaxies).

Indeed, possible spinoffs from this work are the studies of what happens to the resulting structure of merger after losing the ejected particles and of what happens to ejected particles, what is the direction and distribution of the ejection, and the possible effects that these *faster* particles could give to new reached structures, depositing their momenta into them.

Bibliography

A. Arvanitaki and S. Dubovsky. Exploring the string axiverse with precision black hole physics. *Phys. Rev. D*, 83(044026), 2011. arXiv:1004.3558 [hep-th].

E. Barausse, C. Palenzuela, M. Ponce, and L. Lehner. Neutron-star mergers in scalar-tensor theories of gravity. arXiv:1212.5053 [gr-qc], 2012.

P. S. Behroozi, A. Loeb, and R. H. Wechsler. Unbound particles in dark matter halos. *JCAP*, 06(019), 2013. arXiv:1208.0334 [astro-ph.CO].

J. D. Bekenstein. Extraction of energy and charge from a black hole. *Phys. Rev. D*, 7(949), 1973.

D. Bertacca, N. Bartolo, and S. Matarrese. Unified dark matter scalar field models. *Adv. Astron.*, 2010(904379), 2010. arXiv:1008.0614 [astro-ph.CO].

E. Berti, V. Cardoso, and M. Casals. Eigenvalues and eigenfunctions of spin-weighted spheroidal harmonics in four and higher dimensions. *Phys. Rev. D*, 73(024013), 2006. arXiv:gr-qc/0511111.

J. Binney and S. Tremaine. *Galactic Dynamics*. Princeton University Press, 2008.

R. H. Boyer and R. W. Lindquist. Maximal analytic extension of the kerr metric. *J. Math. Phys.*, 8(265), 1967.

C. H. Brans and R. H. Dicke. Mach's principle and a relativistic theory of gravitation. *Phys. Rev.*, 124(925), 1961.

W. F. Buell and B. A. Shadwick. Potentials and bound states. *Am. J. Phys.*, 63(256), 1995.

V. Cardoso. Black hole bombs and explosions: from astrophysics to particle physics. arXiv:1307.0038 [gr-qc], 2013.

V. Cardoso and S. Yoshida. Superradiant instabilities of rotating black branes and strings. *JHEP*, 0507(009), 2005. arXiv:hep-th/0502206.

V. Cardoso, O. J. C. Dias, J. P. S. Lemos, and S. Yoshida. The black hole bomb and superradiant instabilities. *Phys. Rev. D*, 70(044039), 2004. arXiv:hep-th/0404096.

V. Cardoso, I. P. Carucci, P. Pani, and T. P. Sotiriou. Matter around kerr black holes in scalar-tensor theories: scalarization and superradiant instability. arXiv:1305.6936 [gr-qc], submitted to PRD, 2013.

S. M. Carroll. The cosmological constant. *Living Rev. Rel.*, 4(1), 2001. arXiv:astro-ph/0004075.

I. P. Carucci, M. Sparre, S. H. Hansen, and M. Joyce. Particle ejection during mergers of dark matter halos. submitted to JCAP, 2013.

A. J. Cuesta, F. Prada, A. Klypin, and M. Moles. The virialized mass of dark matter haloes. *MNRAS*, 389(385), 2008. arXiv:0710.5520 [astro-ph].

T. Damour and G. Esposito-Farese. Nonperturbative strong field effects in tensor - scalar theories of gravitation. *Phys. Rev. Lett.*, 70(2220), 1993.

T. Damour and G. Esposito-Farese. Tensor - scalar gravity and binary pulsar experiments. *Phys. Rev. D*, 54(1474), 1996. arXiv:gr-qc/9602056.

T. Damour and G. Esposito-Farese. Gravitational wave versus binary - pulsar tests of strong field gravity. *Phys. Rev. D*, 58(042001), 1998. arXiv:gr-qc/9803031.

S. R. Dolan. Instability of the massive klein-gordon field on the kerr spacetime. *Phys. Rev. D*, 76(084001), 2007. arXiv:0705.2880 [gr-qc].

V. Faraoni. *Cosmology in scalar-tensor gravity.* Springer, 2004.

P. C. C. Freire, N. Wex, G. Esposito-Farese, J. P. W. Verbiest, M. Bailes, B. A. Jacoby, M. Kramer, and I. H. Stairs *et al.* The relativistic pulsar-white dwarf binary psr j1738+0333 ii. the most stringent test of scalar-tensor gravity. *MNRAS*, 423(3328), 2012. arXiv:1205.1450 [astro-ph.GA].

Y. Fujii and K. Maeda. *The scalar-tensor theory of gravitation.* Cambridge University Press, 2003.

L. Hernquist. An analytical model for spherical galaxies and bulges. *ApJ*, 356(359), 1990.

W. Israel. Singular hypersurfaces and thin shells in general relativity. *Nuovo Cim. B*, 44S10(1), 1966.

M. Joyce, B. Marcos, and F. Sylos-Labini. Energy ejection in the collapse of a cold spherical self-gravitating cloud. *MNRAS*, 397(775), 2009. arXiv:0811.2752 [astro-ph].

R. P. Kerr. Gravitational field of a spinning mass as an example of algebraically special metrics. *Phys. Rev. Lett.*, 11(237), 1963.

E. W. Leaver. An analytic representation for the quasi-normal modes of kerr black holes. *Proc. Roy. Soc. Lond. A*, 402(285), 1985.

D. Lynden-Bell. Statistical mechanics of violent relaxation in stellar systems. *MNRAS*, 136(101), 1967.

A. V. Maccio', A. A. Dutton, and F. C. van den Bosch. Concentration, spin and shape of dark matter haloes as a function of the cosmological model: Wmap1, wmap3 and wmap5 results. *MNRAS*, 391(1940), 2008. arXiv:0805.1926 [astro-ph].

J. E. McClintock, R. Shafee, R. Narayan, R. A. Remillard, S. W. Davis, and L. Li. The spin of the near-extreme kerr black hole grs 1915+105. *ApJ*, 652(518), 2006. arXiv:astro-ph/0606076.

C. W. Misner. Interpretation of gravitational-wave observations. *Phys. Rev. Lett.*, 28(994), 1972.

P. Pani, V. Cardoso, E. Berti, J. Read, and M. Salgado. The vacuum revealed: the final state of vacuum instabilities in compact stars. *Phys. Rev. D*, 83(081501), 2011. arXiv:1012.1343 [gr-qc].

R. Penrose. Gravitational collapse: the role of general relativity. *Riv. Nuovo Cimento*, 1(252), 1969.

F. Prada, A. Klypin, E. Simonneau, J. Betancort-Rijo, S. Patiri, S. Gottloeber, and M.A. Sanchez-Conde. How far do they go? the outer structure of dark matter halos. *ApJ*, 645(1001), 2006. arXiv:astro-ph/0506432.

W. H. Press and S. A. Teukolsky. Floating orbits, superradiant scattering and the black-hole bomb. *Nature*, 238(211-212), 1972.

C. S. Reynolds. Measuring black hole spin using x-ray reflection spectroscopy. arXiv:1302.3260 [astro-ph.HE], 2013.

L. Sadeghian, F. Ferrer, and C. M. Will. Dark matter distributions around massive black holes: A general relativistic analysis. arXiv:1305.2619 [astro-ph.GA], 2013.

E. Seidel. A comment on the eigenvalues of spin-weighted spheroidal functions. *Class. Quant. Grav.*, 6(1057), 1989.

S. L. Shapiro and S. A. Teukolsky. *Black Holes, White Dwarfs, and Neutron Stars: The Physics of Compact Objects*. Wiley, 1983.

T. P. Sotiriou and V. Faraoni. Black holes in scalar-tensor gravity. *Phys. Rev. Lett.*, 108(081103), 2012. arXiv:1109.6324 [gr-qc].

V. Springel. The cosmological simulation code gadget-2. *MNRAS*, 364 (1105), 2005. arXiv:astro-ph/0505010.

M. Valluri, I. M. Vass, S. Kazantzidis, A. V. Kravtsov, and C. L. Bohn. On relaxation processes in collisionless mergers. *ApJ*, 685(731), 2007. arXiv:astro-ph/0609612.